

REPORT DOCUMENTATION PAGE				Form Approved OMB No. 0704-0188	
<p>Public reporting burden for this collection of information is estimated to average 1 hour per response, including the time for reviewing instructions, searching existing data sources, gathering and maintaining the data needed, and completing and reviewing the collection of information. Send comments regarding this burden estimate or any other aspect of this collection of information, including suggestions for reducing the burden, to Department of Defense, Washington Headquarters Services, Directorate for Information Operations and Reports (0704-0188), 1215 Jefferson Davis Highway, Suite 1204, Arlington, VA 22202-4302. Respondents should be aware that notwithstanding any other provision of law, no person shall be subject to any penalty for failing to comply with a collection of information if it does not display a currently valid OMB control number.</p> <p><b>PLEASE DO NOT RETURN YOUR FORM TO THE ABOVE ADDRESS.</b></p>					
1. REPORT DATE (DD-MM-YYYY) 28-05-2003		2. REPORT TYPE Final Report		3. DATES COVERED (From – To) 7-05-2002 - 7-05-2003	
4. TITLE AND SUBTITLE  High Temperature Protonic Conductors by Melt Growth			5a. CONTRACT NUMBER F61775-02-WE001		
			5b. GRANT NUMBER		
			5c. PROGRAM ELEMENT NUMBER		
6. AUTHOR(S)  Professor Julián Martínez Fernández			5d. PROJECT NUMBER		
			5d. TASK NUMBER		
			5e. WORK UNIT NUMBER		
7. PERFORMING ORGANIZATION NAME(S) AND ADDRESS(ES) Universidad de Sevilla Av/ Reina Mercedes s/n, Apdo. 1065 Seville E-41080 Spain			8. PERFORMING ORGANIZATION REPORT NUMBER  N/A		
9. SPONSORING/MONITORING AGENCY NAME(S) AND ADDRESS(ES)  EOARD PSC 802 BOX 14 FPO 09499-0014			10. SPONSOR/MONITOR'S ACRONYM(S)		
			11. SPONSOR/MONITOR'S REPORT NUMBER(S) SPC 02-4001		
12. DISTRIBUTION/AVAILABILITY STATEMENT  Approved for public release; distribution is unlimited.					
13. SUPPLEMENTARY NOTES					
14. ABSTRACT  This report results from a contract tasking Universidad de Sevilla as follows: The objective of the proposed research is to produce single crystal and multiphase ceramic materials of BaCe1-xNdxO3-a and Ba3(CaNb2)O9 that exhibit high temperature protonic conductance and superior mechanical properties at elevated temperatures. Ba3(CaNb2)O9 material systems will be examined across a broad compositional, and therefore microstructural range, that includes but is not limited to additions of Ga, Nd, and Ta. Characterization will use both Scanning electron microscopy (SEM) and Transmission electron microscopy (TEM). The mechanical behavior BaCe1-xNdxO3-a (x=0 to 0.2) and Ba3(CaNb2)O9 ceramics in the elastic, brittle and plastic regime will be studied over a range of temperatures to 1300°C. Impedance spectroscopy will be used to study mass transport of charged particles (protonic conductance). The spatial variations of compositions in BaCe1-xNdxO3-a and Ba3(CaNb2)O9 following high temperature wet atmosphere treatment will be measured using a variety of techniques based on the nuclear microprobe.					
15. SUBJECT TERMS EOARD, Materials, Fuel Cells, Ceramics					
16. SECURITY CLASSIFICATION OF:			17. LIMITATION OF ABSTRACT UL	18. NUMBER OF PAGES  45	19a. NAME OF RESPONSIBLE PERSON Charles H. Ward, Lt Col, USAF
a. REPORT UNCLAS	b. ABSTRACT UNCLAS	c. THIS PAGE UNCLAS			19b. TELEPHONE NUMBER (Include area code) +44 (0)20 7514 3154

**HIGH TEMPERATURE PROTONIC CONDUCTORS BY MELT GROWTH  
PURCHASE ORDER NO. F61775-02-WE001, SPC-02-4001**

**FINAL REPORT**

This material is based upon work supported by the European Office of Aerospace Research and Development, Air Force Office of Scientific Research, Air Force Research Laboratory, under Contract No. F61775-02-WE001

Any opinions, findings and conclusions or recommendations expressed in this material are those of the author(s) and do not necessarily reflect the views of the European Office of Aerospace Research and Development, Air Force Office of Scientific Research, Air Force Research Laboratory.

**Institutions involved:** University of Seville (US), Ecole de Mines de Paris (ARMINES), Commissariat à l'Energie Atomique (CEA), and Case Western Reserve University (CWRU)

**Fabrication of protonic conductors**

High temperature protonic conductors (HTPC) were successfully fabricated by melt growth using the laser heated floating zone method. Simple perovskites with several tetravalent atoms and amounts of trivalent dopant were produced ( $\text{SrCe}_{0.9}\text{Y}_{0.1}\text{O}_{3-\delta}$ ,  $\text{SrCe}_{0.8}\text{Y}_{0.2}\text{O}_{3-\delta}$ ,  $\text{SrZr}_{0.9}\text{Y}_{0.1}\text{O}_{3-\delta}$ ,  $\text{SrZr}_{0.8}\text{Y}_{0.2}\text{O}_{3-\delta}$ , and  $\text{SrTi}_{0.95}\text{Sc}_{0.05}\text{O}_{3-\delta}$ ).

Mixed perovskites type  $\text{Sr}_3(\text{CaNb}_2)\text{O}_9$ , with two values of stoichiometry were also produced ( $\text{Sr}_3(\text{Ca}_{1.18}\text{Nb}_{1.82})\text{O}_{9-\delta}$  and  $\text{Sr}_3(\text{Ca}_{1.3}\text{Nb}_{1.7})\text{O}_{9-\delta}$ ). Typical size of the rods produced was 4 mm of diameter by 100 mm of length.

For preparation of the source rod, high purity (99.999% pure) polycrystalline  $\text{SrCO}_3$  powder, high purity (99.999% pure) polycrystalline  $\text{CeO}_2$  and  $\text{Y}_2\text{O}_3$  (pure) were obtained from CERAC/pure<sup>†</sup> (325 mesh). This powder was blended and milled without milling agents 40 hours. The powder mixture is then calcined at 800 °C in air for 6 hours. The calcined samples crushed and sieved and calcining step is repeated. The powders are cold isostatically pressed into the cylindrical rods and sintered in air at 1500 °C. The rods were placed in the laser heated float zone apparatus and rods are grown directly from the source material in air.

The laser heated floating zone apparatus is intended to be a fully automatic, computer controlled, fiber processing facility. For the heating source, a coherent  $\text{CO}_2$ -laser beam (PRC 2200)<sup>#</sup> was used. The laser was split into two beams, 180° apart from each other. Each beam was then focused with zinc-selenide lenses onto the molten zone at the top of a polycrystalline source rod in the center of the processing chamber. These opposing beams are converted into opposing laser line scans. The line scans are produced by reflecting the focused laser beam on a rotating cams (gold-plated). The larger diameter area of the feed rod intercepts a greater amount of the laser energy which is necessary for it to be preheated and made molten, then as the diameter of the molten zone reduces down to the growing material less laser energy is intercepted thereby preserving the solid liquid interface. The source rod can move vertically

---

<sup>†</sup> Ceralox Corp., Tucson, AZ 08576.

<sup>#</sup> PRC CORP., Landing NJ 0785.

through the laser beam and its motion was computer-controlled. The maximum available laser power was 2200 watts, but only a small fraction of this power (800 to 1100 watts) was needed because most of the radiation from the CO<sub>2</sub>-laser (wavelength=10.6 μm) is absorbed in the oxides. The molten zone temperature, which was measured in the infrared radiation region with a custom made Infrared Thermal Monitor,<sup>+</sup> was used to control the laser power. Absolute temperature, however, was not measured because the emissivity of the molten mixture was not known. All experiments were conducted in air. Neither the crystal nor the source rod was rotated. A TV monitor facilitates the control of seeding and crystal growth. In addition to TV monitors, a Questar 100 long range optical microscope and a high resolution Kodak Camera were used and linked to a desktop computer.

### **Microstructural characterization**

Microstructural characterization was performed by optical and electron microscopy. The materials presented a cellular structure with an intergranular phase. The cells/grains are wider and less aligned with the growth axis, when closer to the rod center. The cell width ranges between 10-50 μm and the aspect ratios are roughly up to 10. The best quality crystals were obtained for the system SrCe<sub>0.9</sub>Y<sub>0.1</sub>O<sub>3-δ</sub>.

### ***Optical microscopy***

Their external appearance is shown in Fig 1. They have a green colour, a diameter of 3 to 4 mm. Their surfaces show periodic lines (periodicity around 200 μm on the left of Fig 1), the orientations of which reflect the shape of the liquid/solid interface during solidification. On a longitudinal section, Fig 2, a core / rim contrast is revealed, the central part (around 1.2 mm) being brighter than the outer part.

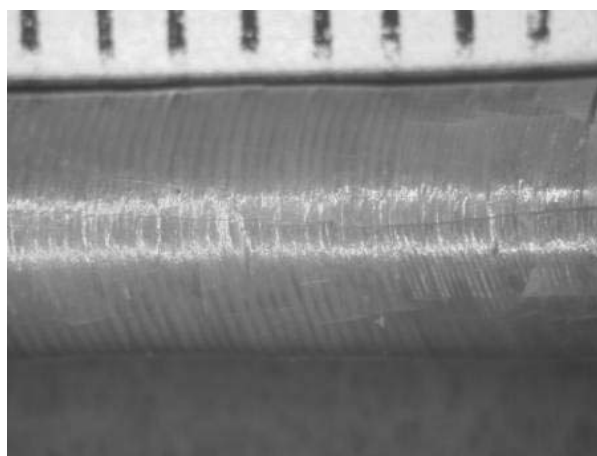


Fig 1: External appearance of rod SrCe<sub>0.9</sub>Y<sub>0.1</sub>O<sub>3-δ</sub> obtained by oriented solidification.  
1 graduations / mm

---

<sup>+</sup> Vanzetti Systems, Stoughton, MA 02072.

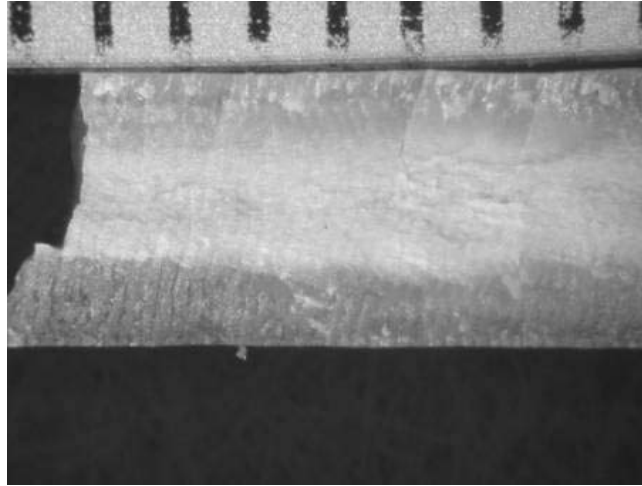


Fig 2: Longitudinal section. 1 graduations / mm

### ***Scanning electron microscopy (SEM)***

Longitudinal sections were polished using SiC papers (1200 – 2400 – 4000) and finally with OPS solution (colloidal silica + KOH).

Figs 3 and 4 show images of polished longitudinal sections obtained by optical microscopy and SEM respectively. They reveal three regions when going from the outer to the central parts of the section:

**Zone 1:** On a thickness of around 500  $\mu\text{m}$  from the surface, the microstructure is composed of large regions with only a small amount of second phase inclusions alternating periodically with regions containing elongated thin second phases. This microstructure is shown in more detail in Fig 5. Each region has a width of around 100  $\mu\text{m}$ . They are slightly disoriented with respect to the rod diameter, which reflects the curvature of the solid liquid interface during solidification.

**Zone 2:** The thickness of this intermediate zone is around 400  $\mu\text{m}$ . It is composed of elongated grains (length  $\approx 200$   $\mu\text{m}$  width  $\approx 25$   $\mu\text{m}$ ), separated by a second phase, **Fig 6**.

**Zone 3:** The core of the rod is composed of grains with lower aspect ratios and wavy boundaries. The intergranular second phases are thicker as shown by **Fig 7**. The radius of this central zone is around 700  $\mu\text{m}$



Fig 3: Longitudinal section. Optical image. Three zones are revealed.

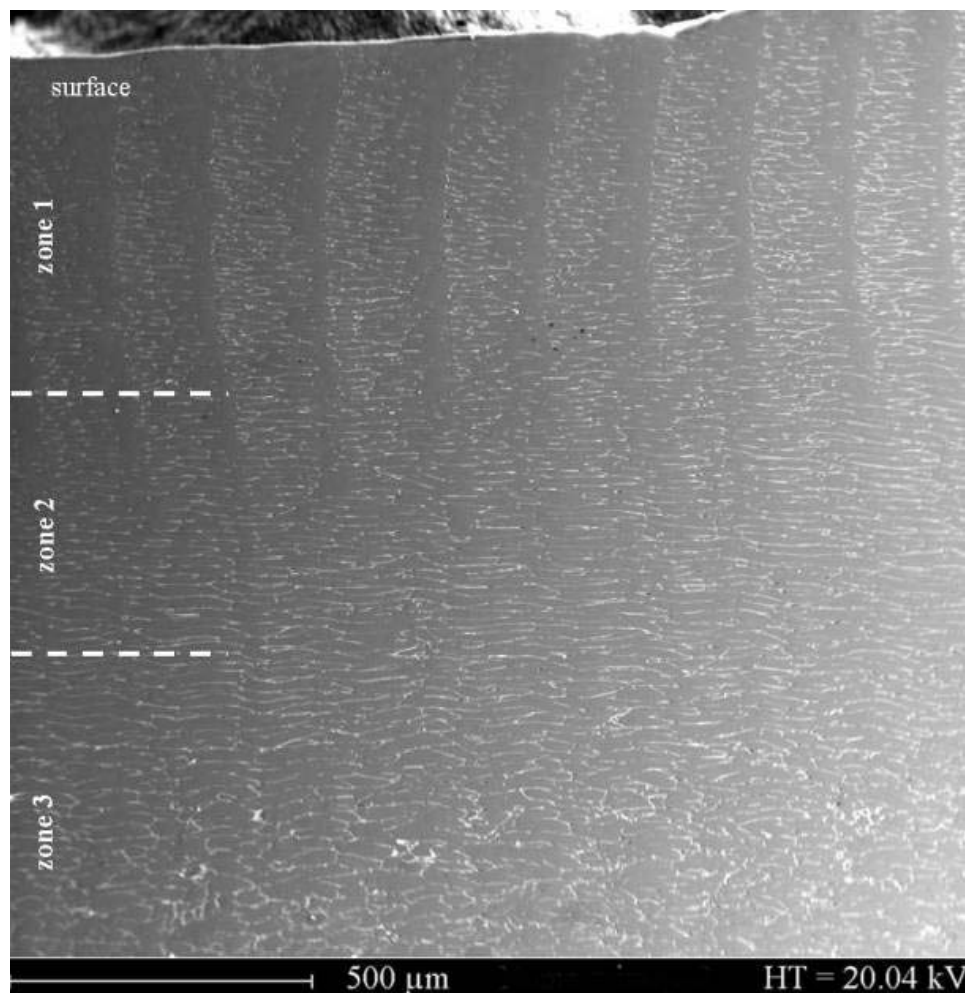


Fig 4: Longitudinal section. SEM image. The white contrast of the boundaries is due to a preferential etching of the boundaries during OPS polishing causing topographic steps and accumulation of electrical charges

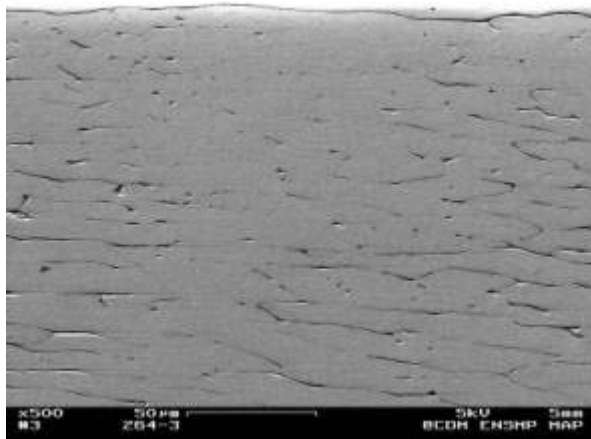


Fig 5: Aspect of Zone 1

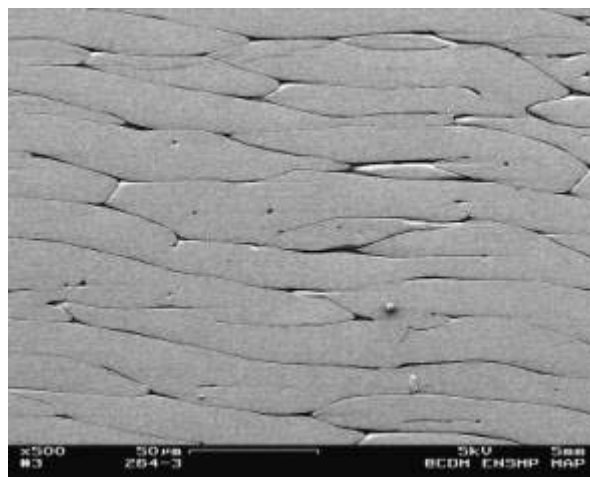


Fig 6: Aspect of Zone 2

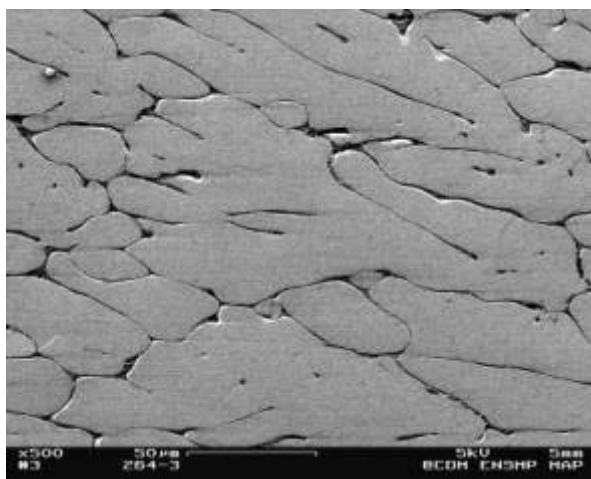


Fig 7: Aspect of Zone 3

### *Electron microprobe analyses*

Chemical analyses have been done using electron microprobe (WDX mode).

The calibration samples used for quantitative analyses were:

O and Sr :  $\text{SrSO}_4$  - Ce:  $\text{CeAl}_2$  - Y: Y metal - F apatite mineral (O 38.9, Ca 32.02, P 18.32 F 3.40 Cl 0.35 wt%), Al:  $\text{Al}_2\text{O}_3$  .

**Table 1** gives an average value of 10 analyses carried out on windows of  $50 \times 50 \mu\text{m}^2$  on each of the three zones.

	Sr	Ce	O	Y	Al	F	Total
<b>10 analyses on <math>50 \times 50 \mu\text{m}^2</math> Zone 1 (surface)</b>							
Mean Weight %	29.70	46.14	16.65	3.45	0.07	0.41	96.42
Stand. dev	0.34	0.67	0.18	0.13	0.04	0.10	0.55
Mean Atomic %	19.13	18.59	58.73	2.19	0.14	1.21	

Stand. dev	0.13	0.38	0.29	0.08	0.09	0.30	
<b>10 analyses on 50*50 <math>\mu\text{m}^2</math> Zone 2 (intermediate)</b>							
Mean Weight %	29.58	44.95	17.36	3.55	0.25	0.41	96.09
Stand. dev	0.17	0.87	0.28	0.13	0.10	0.09	0.61
Mean Atomic %	18.61	17.69	59.82	2.20	0.51	1.17	
Stand. dev	0.17	0.48	0.40	0.06	0.21	0.27	
<b>10 analyses on 50*50 <math>\mu\text{m}^2</math> Zone 3 (core)</b>							
Mean Weight %	29.52	44.22	17.62	3.74	0.43	0.41	95.94
Stand. dev	0.38	0.83	0.40	0.18	0.17	0.09	0.50
Mean Atomic %	18.38	17.22	60.06	2.29	0.86	1.18	
Stand. dev	0.37	0.54	0.67	0.09	0.33	0.26	

Table 1: WDX analyses on 50\*50  $\mu\text{m}^2$ .

The total weight percentage reaches  $\approx 96\%$ . The weight to atomic conversion is calculated on the basis of a total atomic % of 100.

It is suspected that topographic irregularities on these windows are responsible for the 4% mismatch in the total weight percentage. The following spot analyses done on the centers of grains or second phases give better results (Table 2)

Local analyses have been done a large intergranular pocket (zone 3), on a large region crystalline (zone 1) and on a large grain (zone 3). The widths of these zones have been chosen in order to minimize any intersection of the interaction zone (diffusion length 2  $\mu\text{m}$  at 20 kV) with the adjacent grains or second phases. The following weight and atomic ratios have been measured:

	Sr	Ce	O	Y	Al	F	total
<b>2<sup>nd</sup> phase</b>							
Weight %	32.00	34.11	23.66	4.85	3.97	0.20	98.81
Atomic %	15.88	10.58	64.30	2.37	6.39	0.46	
<b>grain zone 1 (surface)</b>							
Weight %	30.46	46.59	16.31	3.65	0.09	0.50	97.59
Atomic %	19.64	18.78	57.58	2.32	0.19	1.48	
<b>grain zone 3 (core)</b>							
Weight %	30.60	47.71	16.26	3.49	0.02	0.40	98.48
Atomic %	19.76	19.27	57.51	2.22	0.04	1.19	

Table 2 WDX local analyses. Interaction range 2 $\mu\text{m}$ .

The composition that was aimed when growing these samples was:

Table 3 : Nominal composition $\text{SrCe}_{0.9}\text{Y}_{0.1}\text{O}_{2.95}$				
	Sr	Ce	O	Y
Atomic %	20.20	18.18	59.60	2.02

The oxygen content has been calculated with the hypothesis that all the Y cations occupy the Ce sites.

From these windows and local analyses it can be concluded

1°) The grains have a lower Sr/Ce ratio (1.05-1.02) than that of the nominal composition (1.1). This ratio is higher in the second phase (1.5). The average ratios measured in the three zones on the window analyses (zone 1: 1.03-zone: 2 1.05- zone 3: 1.07) show that a preferential evaporation of SrO during the growth may have occurred.

2°) A contamination by Al and F cations is revealed. Alumina boats used to sinter the source rods might explain the Al contamination.

3°) Al is clearly concentrated in the second phase whereas F is more homogeneously distributed.

3°) The compositions of the grains in the core and in the outer region are comparable. A larger number of analyses would be necessary to see if the differences registered are significant.

4°) The differences in the mean compositions found in the window analyses going from the core to the center reflect a progressive enrichment in second phase and lower Sr evaporation level.

Secondary electron images and Al, Sr, Ce, O, Y chemical images are shown in Fig 8 to 10 to illustrate the distribution of these elements. (F maps have not been added, the distribution of this element is homogeneous at the scale of the analyses)



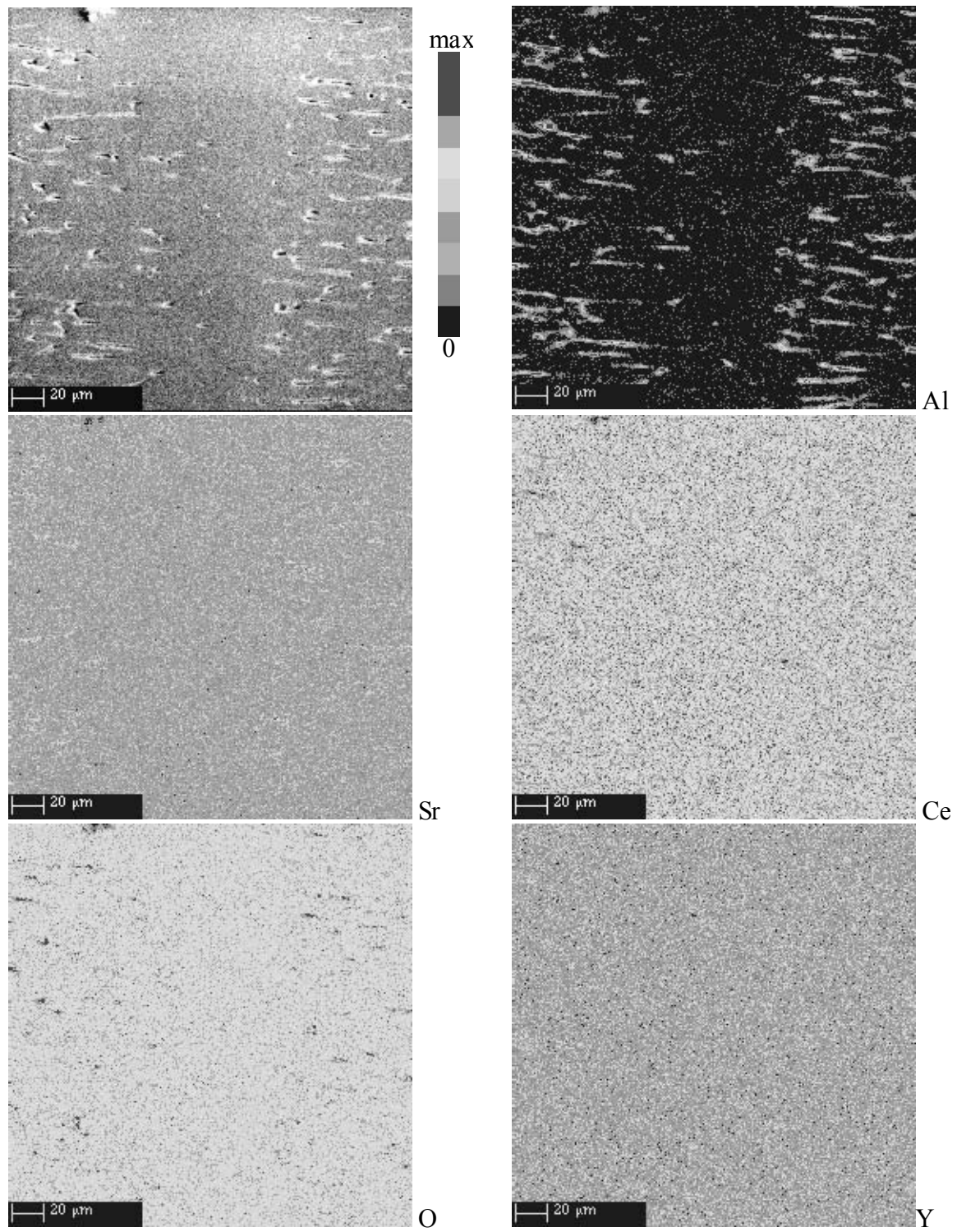


Fig 8: Zone 1. Large homogeneous zones.

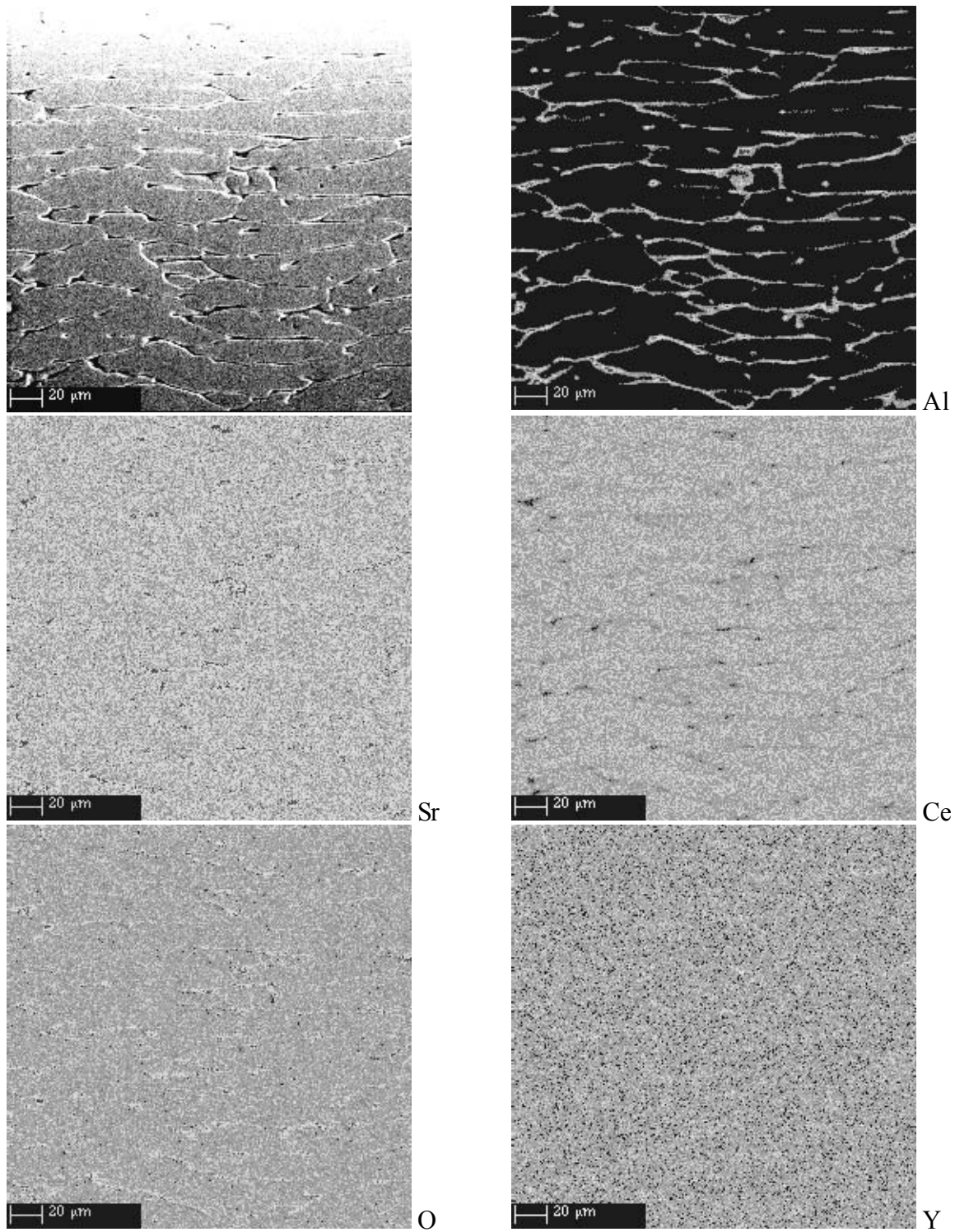


Fig 9: Zone 2. Intermediate zone with elongated grains.

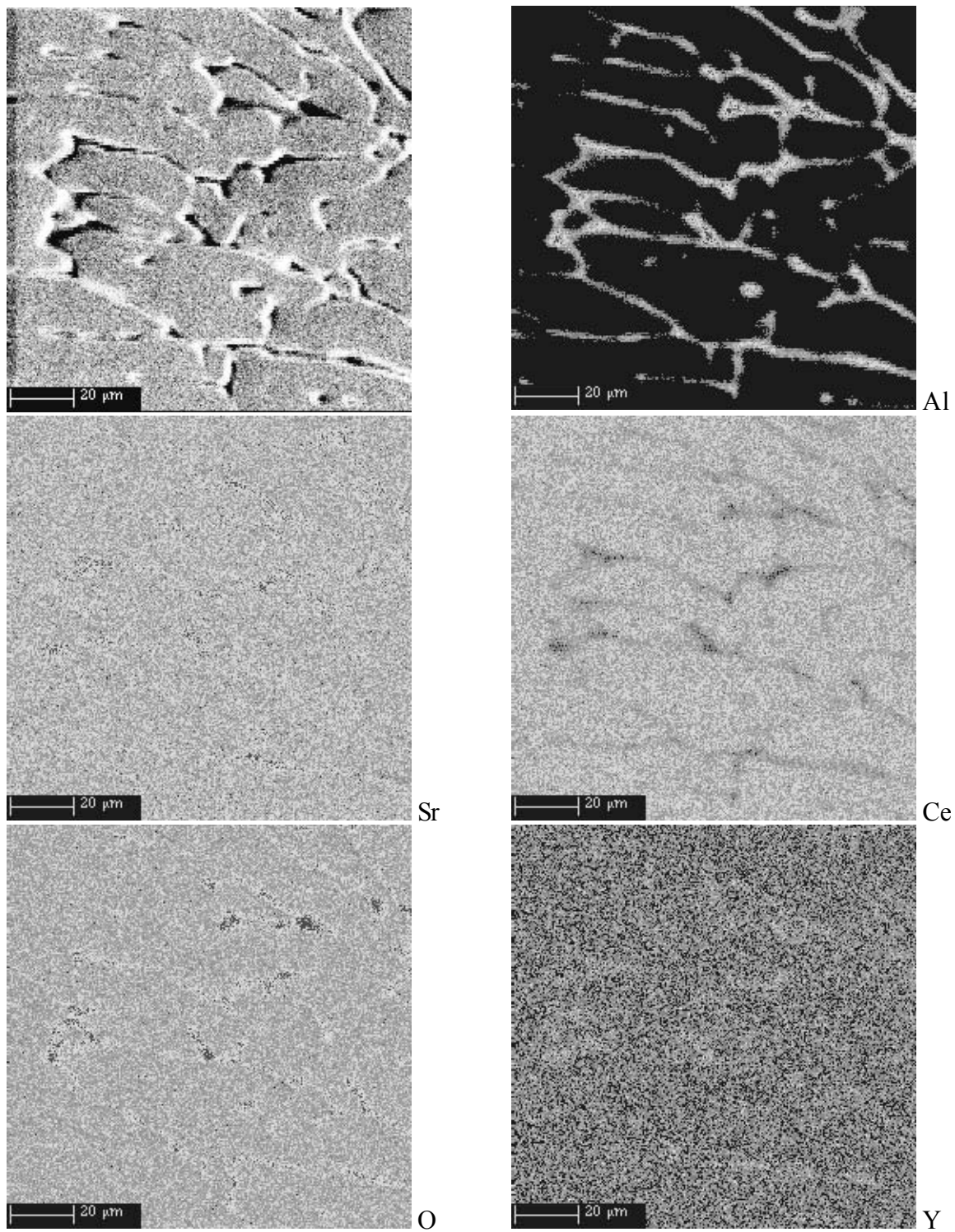


Fig 10: Zone 3 - Core of the sample. Grains are less elongated second phases thicker.

### ***Transmission electron microscopy (TEM)***

The grains and the intergranular phase observed by SEM can be easily identify in the TEM micrographs of Fig. 11. The grains present multiple planar defects and curved features (arrowed). The intergranular phase shows a contrast without crystallographic defects and only a dotted texture that could be due to voids or thinning damage.

The diffraction analysis (Fig. 12) indicate that the grains are crystalline (Fig. 12 B-E), and the intergranular phase is amorphous (Fig. 12 F). The diffraction patterns are consistent with a perovskite structure with a reticular parameter of  $8.53 \pm 0.04 \text{ \AA}$ . This parameter is in the range of the literature values.

The preliminary analysis indicate that the planar defects separate regions with the same crystallographic structure and orientation, but with different systematic extinctions in the diffraction pattern. Fig. 12B and 12C shows the diffraction patterns in both sides of a planar defect that can be identify as (100). Fig. 12 E shows a diffraction pattern from both regions. The spots of these diagrams are indexed in Fig. G and H. The only difference between them is that in one there are extra f.c.c. type extinctions and the relative intensities of the spots are not the same. The differences in the patterns could be due to small changes in dopant distribution that causes slight differences in the atomic arrangement of the unit cell. Further studies are necessary to reach definitive conclusions.

Within the grain it is common to find “precipitates” like the one shown in Fig. 13. The diffraction patterns have also different systematic extinctions as occurred in the patterns shown above.

The EDX microanalysis (Fig. 14) performed in the grains and in the intergranular regions, show similar results to those obtained by SEM. It is particularly clear the larger Ce content in the crystalline region and the larger Al content in the amorphous intergranular region.

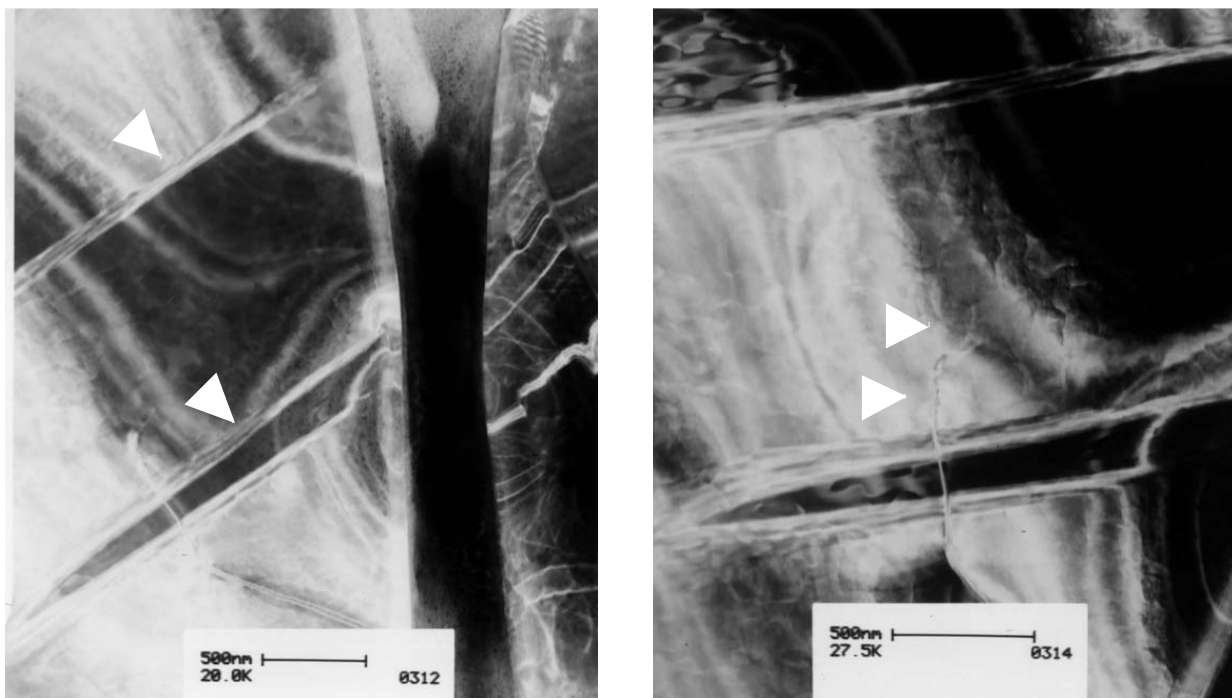


Fig 11: TEM micrographs of the as-fabricated samples

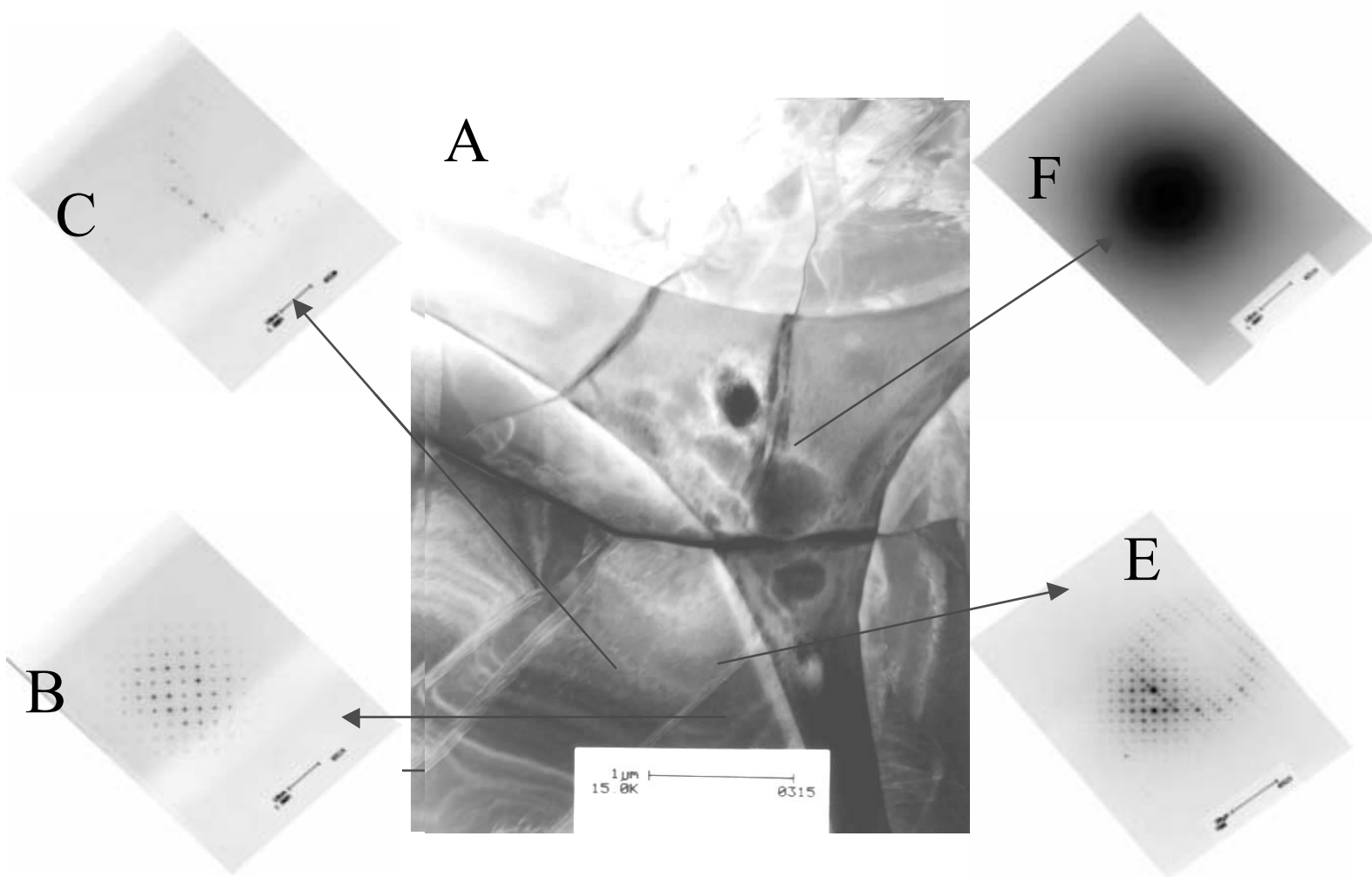


Fig 12: A-F) Electron diffraction analysis of the grains and intergranular phase.

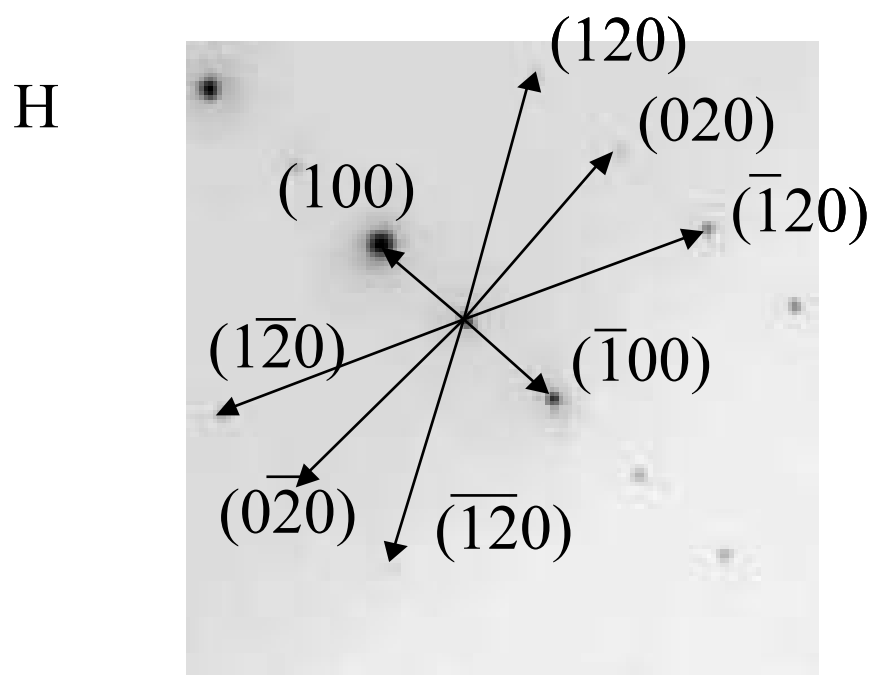
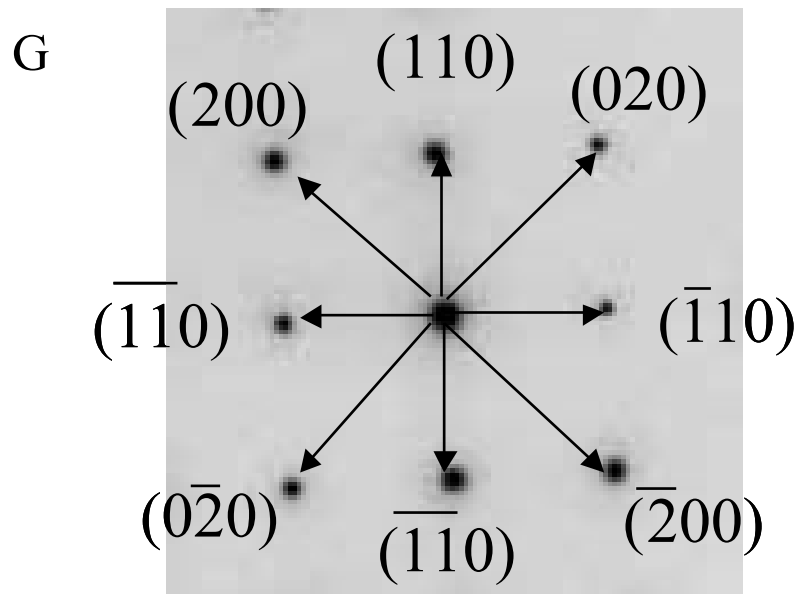


Fig. 12: G) Solution of diagram B, H) solution of diagram C

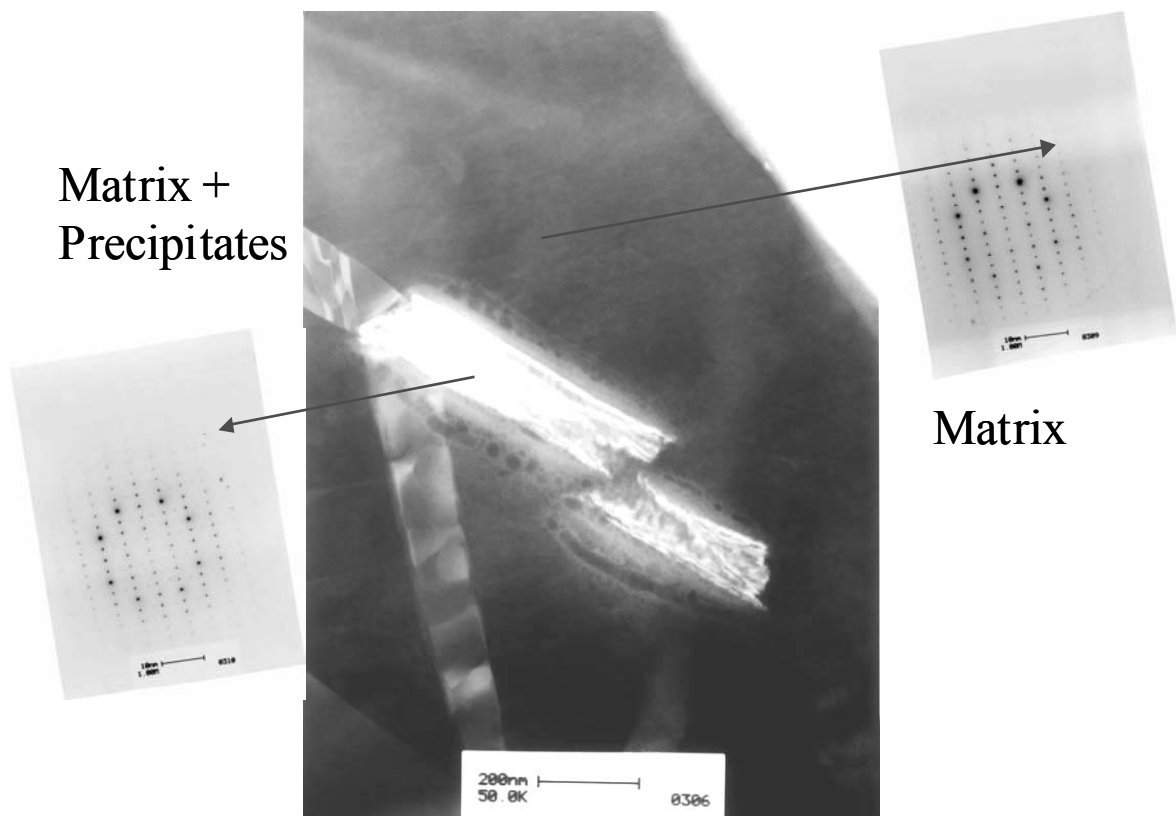


Fig. 13: Electron diffraction analysis of an intragranular precipitate

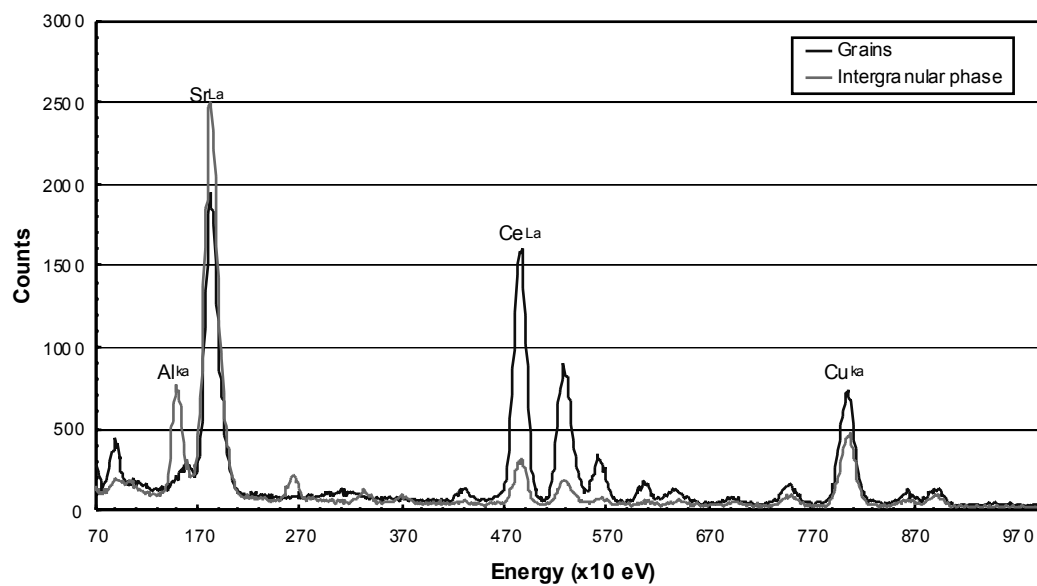


Fig. 14: EDX analysis of the grains and intergranular region



## High Resolution Transmission Microscopy (HRTEM)

High-resolution TEM images on  $\text{Sr}_3(\text{Ca}_{1.18}\text{Nb}_{1.82})\text{O}_{9.8}$  were obtained using the OAM (One Ångström resolution Microscope) of the National Center for Electron Microscopy, Lawrence Berkeley Laboratory.

The aim of these observations was to look for any ordering in sublattices of Ca and Nb cations on the B site, black circle on the right image, which is known to influence the proton mobility in the perovskite structure\*.

The distribution of the B cations in  $\text{A}_3(\text{B}'_{1+x}\text{B}''_{1-x})\text{O}_9$  perovskites can be random or ordered. In the last case two periodic sequences are described.

1:1 compounds:

In the direction normal to  $[111]_p$  direction of the perovskite unit cell planes of B' alternate with planes of B''.

1:2 compounds:

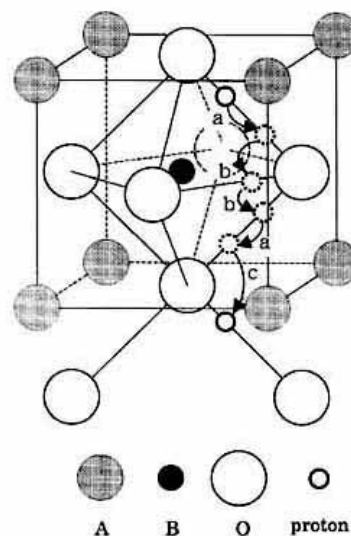
In the direction normal to  $[111]_p$  direction of the perovskite unit cell, a plane of B' alternates with two planes of B''. This distribution corresponds to the so called 1:2 order. Galasso<sup>†</sup> and Pyle have described  $\text{Sr}_3(\text{CaNb}_2)\text{O}_9$  (jcpdf 17-164) using this cation distribution.

Depending on the value of x, these ordered structures can coexist (clusters of 1:1 in 2:1 lattice for example) or regions with a random distribution can be found around 1:1 domains.

Another description of  $\text{Sr}_3(\text{CaNb}_2)\text{O}_9$  was proposed by Hervieu and Raveau<sup>‡</sup>. The lattice is tetragonal with almost identical *a* and *c* parameters:  $a_T = 8.190 \text{ Å}$ ,  $b_T = 8.209 \text{ Å}$ , the group of symmetry is P-4 (81), jcpdf card number: 71-1109. This description of the structure corresponds to a doubling of the perovskite unit cell  $a_T \approx 2 a_p$ ,  $b_T \approx 2 b_p$ . In the direction normal to  $[111]_p$ , planes only occupied by Nb alternate with planes occupied randomly by calcium and niobium.

The oxygen non-stoichiometry required to introduce protons in the structure is obtained by a substitution some  $\text{Nb}^{5+}$  by  $\text{Ca}^{2+}$  to produce the protonic conductor phases  $\text{Sr}_3(\text{Ca}_{1+x}\text{Nb}_{2-x})\text{O}_{9.8}$ . In our case the composition of the feed material used in the directionally solidification was chosen to result in  $x=0.18$ .

Figure 15 shows a high resolution image obtained in 001 zone axis and the corresponding the FFT (Fast Fourier Transform). The indexation of the pattern can be done using an average unit cell of the simple perovskite. This high-resolution image and the associated diffraction pattern do not show any superstructure. No ordering of the cations is revealed. The distributions of Ca and Nb cations on the B sites are random in this region.



\* Nowick A.S., Du Y., Liang K.C. Solid State Ionics 125 303 (1999)

† Galasso, Pyle J. Phys. Chem. 67, 1561, (1963),

‡ Hervieu M, Raveau B, J Solid State Chem, 28, 209, (1979)



Figure 16 shows another region of the crystal in the same zone axis. On the associated FFT, the doubling of the unit cell is shown by additional spots on  $[100]^*$  (yellow circle).

In Fig 17 two  $90^\circ$  domains with a doubling respectively on a and b directions are imaged.

In Fig 18 and 19 the doubling of the parameter is seen on  $[110]^*$

The two sequences of cations ordering observed along  $[100]$  and  $[110]$  are illustrated in Fig 20. They correspond to a 1:1 ratio of Ca and Nb, whereas the average Ca/Nb ratio in the sample is close to 1.54. These domains of 1:1 order are hence associated with compositional partitioning. These chemical variations are seen in domains very close to each other separated by domains with higher degree of disorder.

Similar compositions,  $\text{Sr}_3\text{Ca}_{1+x}\text{Nb}_{2-x}\text{O}_{9-\delta}$  have been studied in conventional TEM microscopy and SAD diffraction by Nowick et al.,. They show two ordering sequences one along  $[100]$  corresponding to a 1:1 order, one along  $[111]$  corresponding to a 1:2 order. The types of order change with increasing x, going from “1:2” to “1:1 + random”. They report that higher proton apparent motilities are obtained when the 1:1 ordering mode is dominant. The onset of 1:1 order occurs at higher x ( $x > 0.2$ ) than in our study  $x = 0.18$ . The average chemical composition of our sample has to be obtained before interpreting these differences in terms of process conditions. Conventional TEM on larger areas will be carried out together with EDX analysis to follow local Ca/Nb variations.

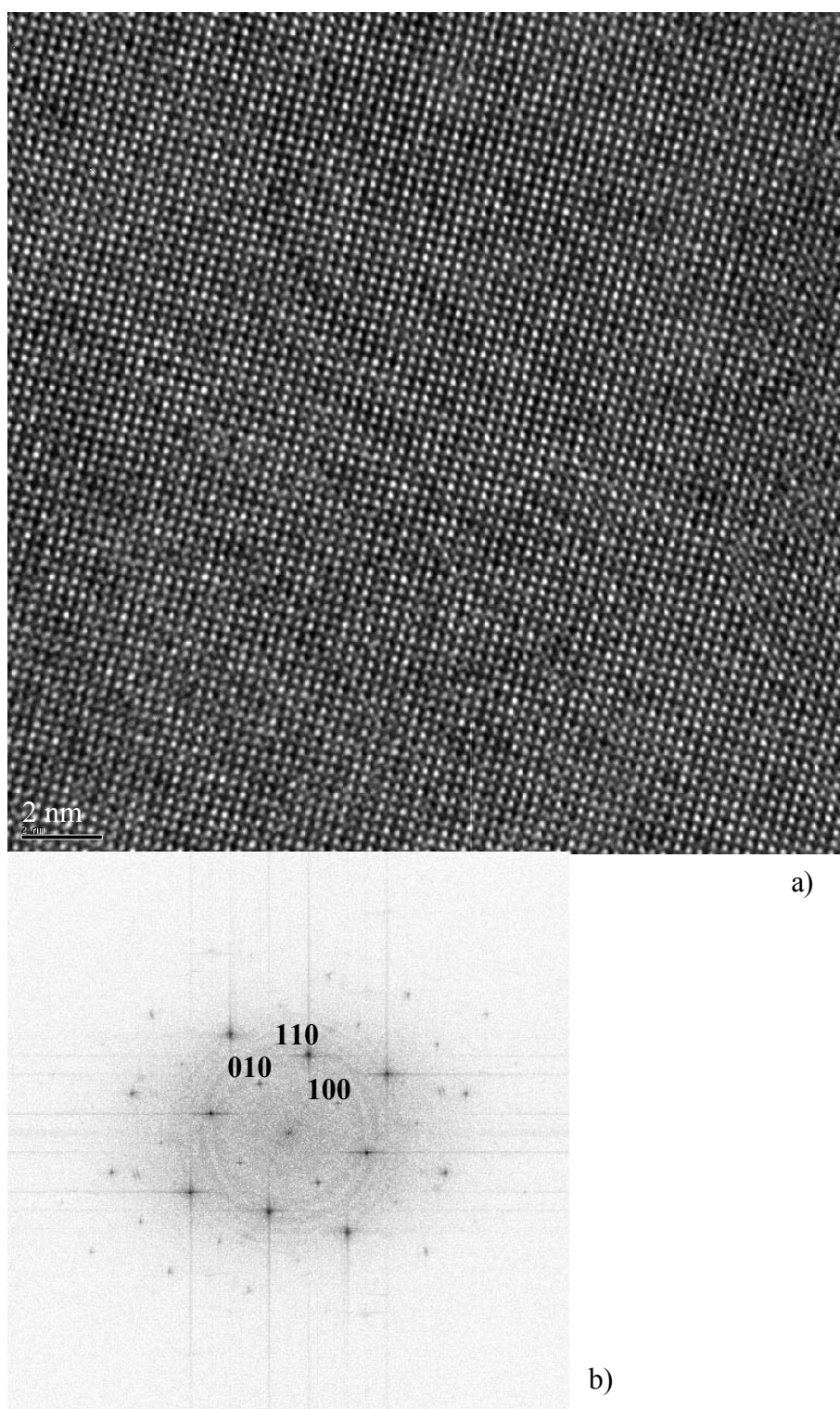
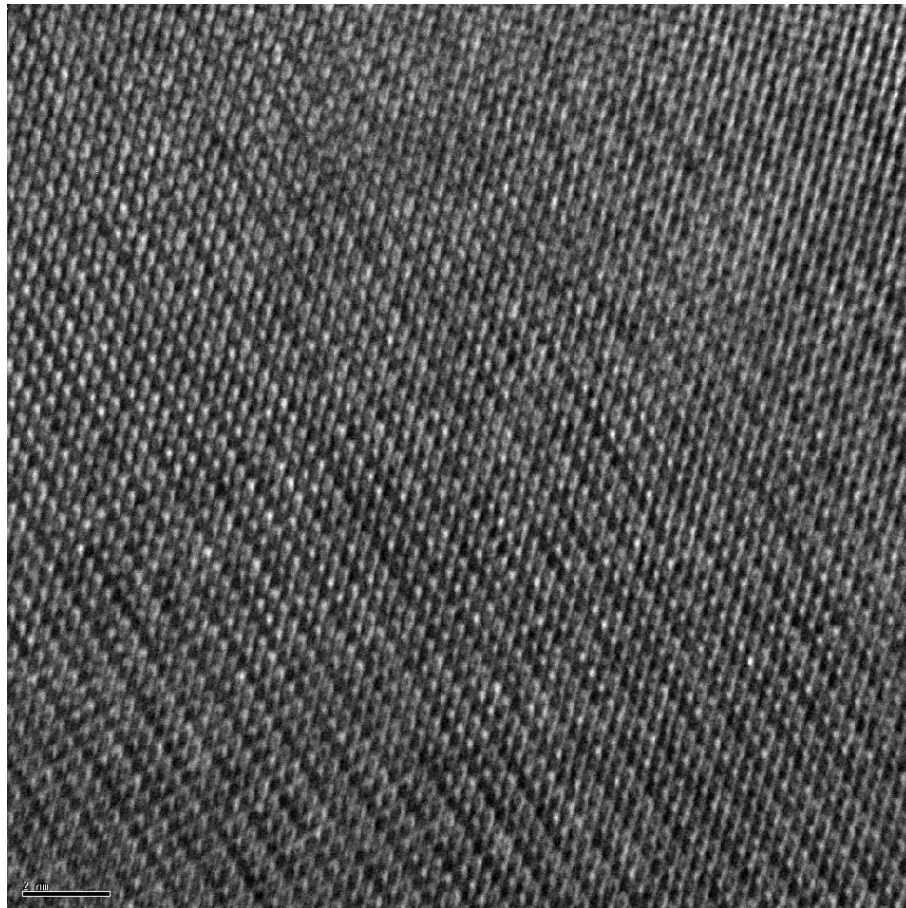
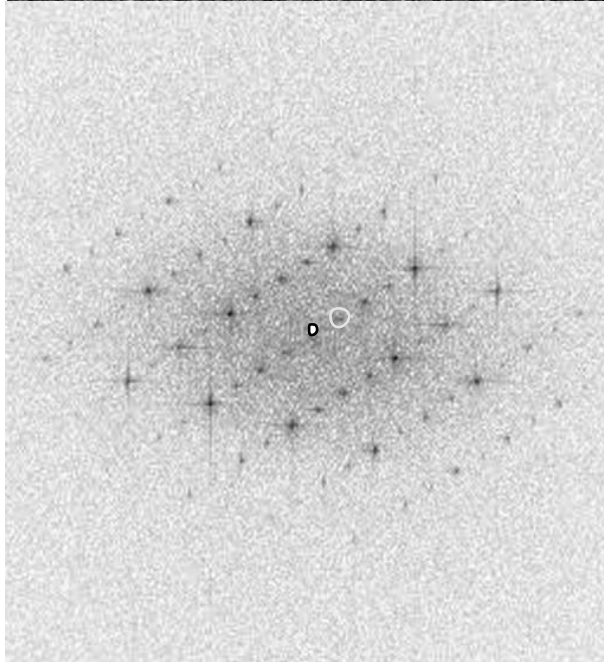


Fig 15 : Random distribution of Ca and Nb. The FFT is similar to that of a simple perovskite in the [001] zone axis with  $a=3.89 \text{ \AA}$ . No superlattice reflexion is revealed.

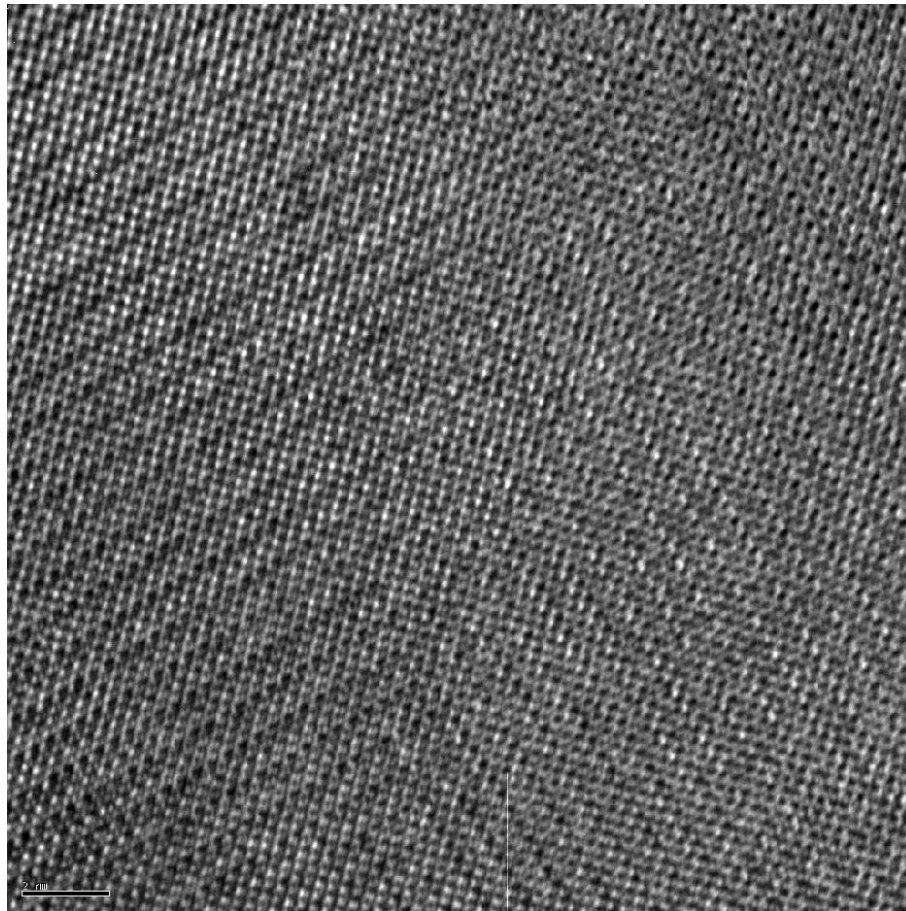


a)

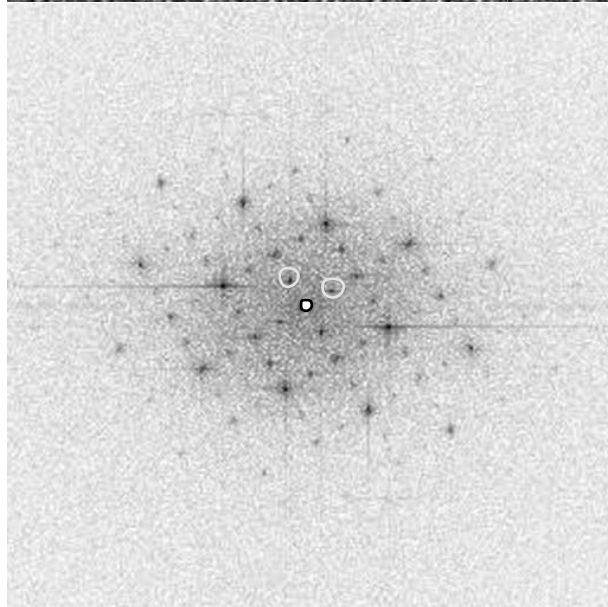


b)

Fig 16 : Superlattice modulation, ordering along  $[100]$

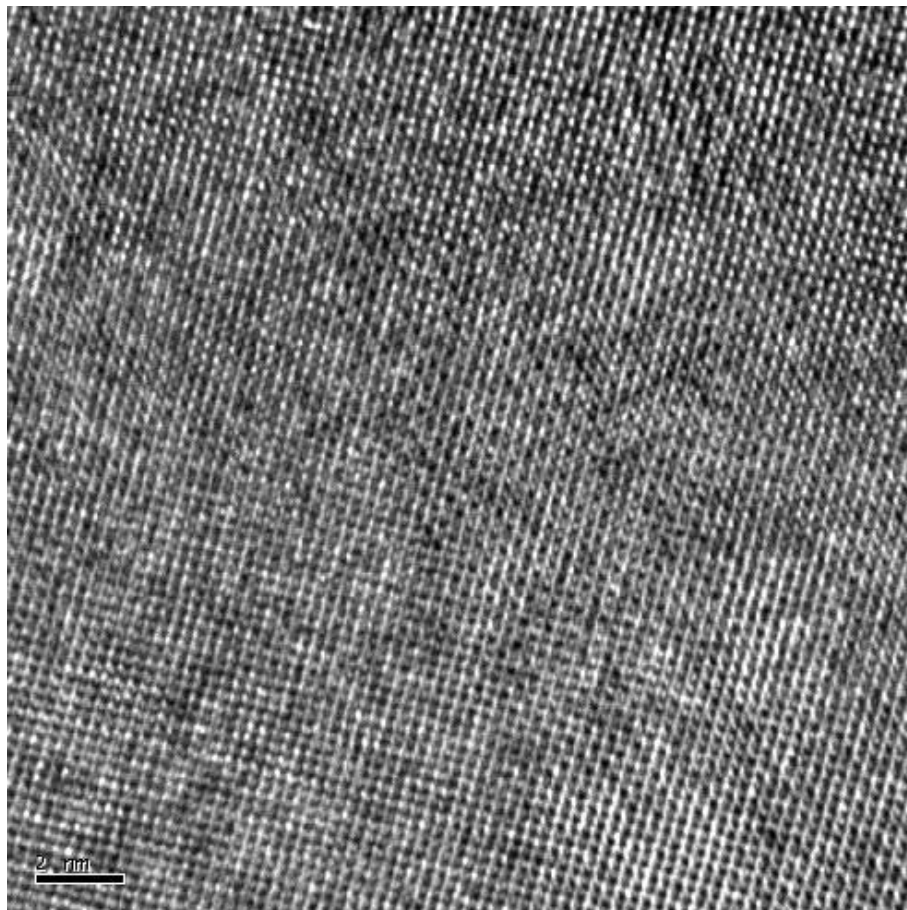


a)

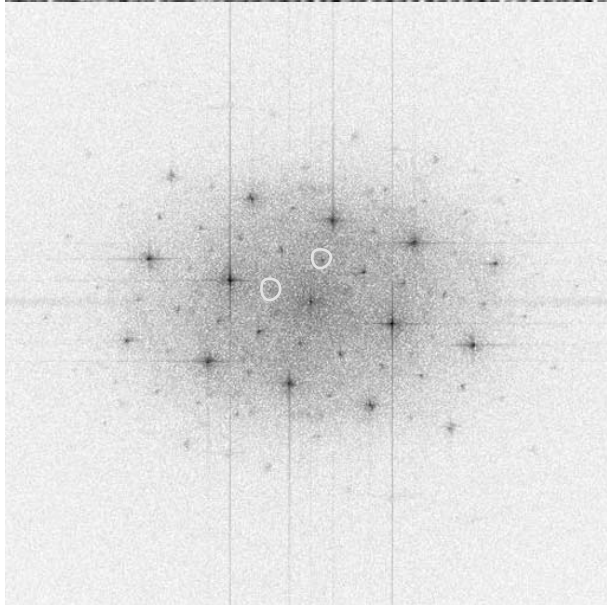


b)

Fig 17 : Two 90° domains with ordering along  $[100]$  and  $[010]$

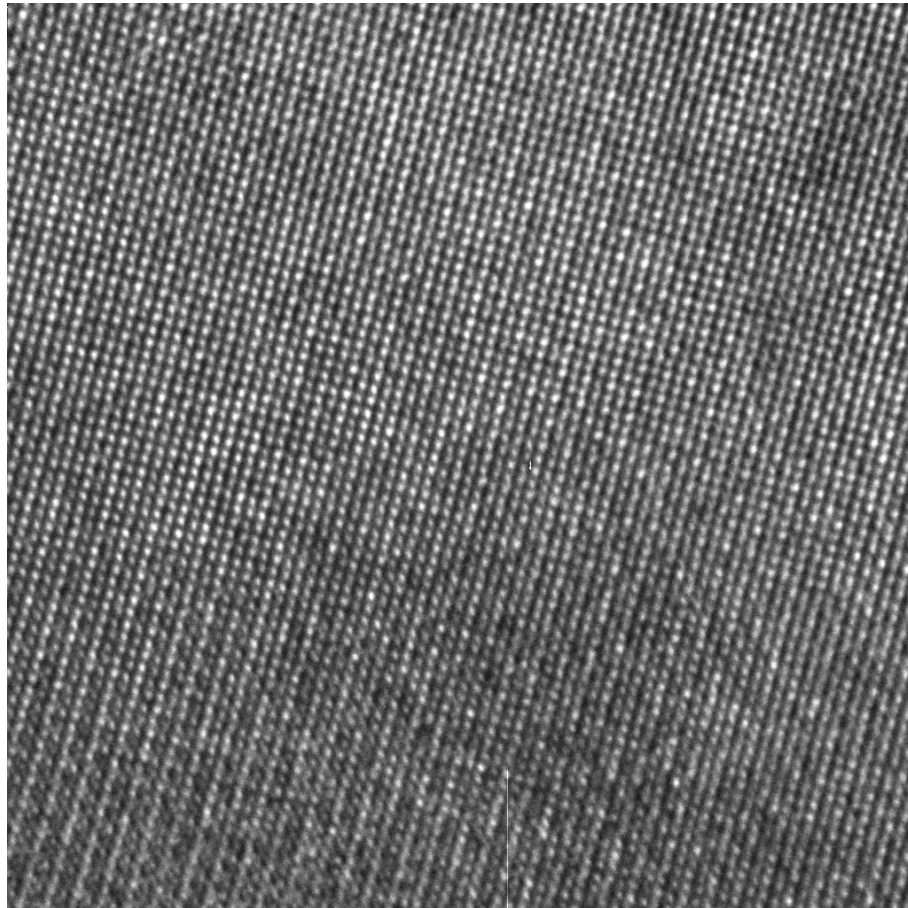


a)

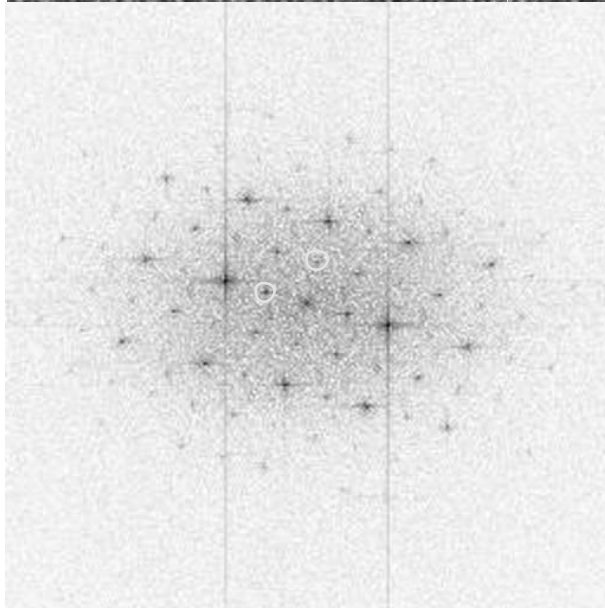


b)

Fig 18 : Ordering along  $[110]$  and  $[1-10]$



a)



b)

Fig 19: Ordering along  $[110]$  and  $[1-10]$

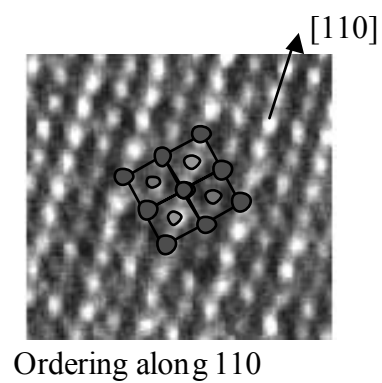
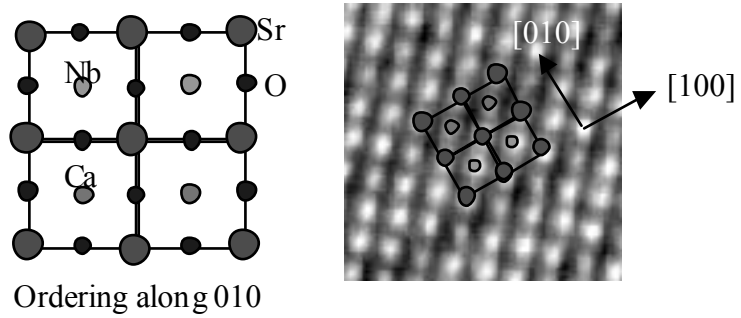


Fig 20 : Schematic representation of the B' – B'' distributions observed



## **High Temperature Mechanical Properties**

The bars of HTPC were cut in cylinders of 5 mm in length and typically 4 mm of diameter. The compressive strength was measured at a constant strain rate of 5 micron /minute (equivalent to  $1.5 \times 10^{-5} \text{ s}^{-1}$  for our sample dimensions) for temperatures up to 1300 °C in air. Testing was performed using a screw driven universal testing machine (Microtest EM1/50/FR, Madrid, Spain) with a furnace mounted on its frame (Fig 21).

Remarkable high temperature strengths of 500 MPa at 700 °C, 400 MPa at 1100 °C and 370 MPa at 1300 °C were measured. At room temperature and 700 °C sudden catastrophic failure was found and the samples were reduced to powder after the tests, what may indicate that the material failed due to its internal cracks (Fig. 22).

Fig. 23 shows stress-strain curves at 1300 °C for all the materials studied. The maximum strength ranges from 120 to 370 MPa, being  $\text{Sr}_3(\text{Ca}_{1.18}\text{Nb}_{1.82})\text{O}_{9.8}$  the strongest system. It is remarkable that in this first batch of samples high strengths are achieved, being predictable a reproducible strength around 400 MPa at 1300 °C when an optimum fabrication route is determined.

The strengths are very high when compared with polycrystalline high temperature protonic conductors of similar structure/composition. Fig. 24 plots the strength versus temperature for our system together with the data from Park et al [Solid State ionics 117 (1999) 323-330] in polycrystalline  $\text{BaCe}_{0.9}\text{Y}_{0.1}\text{O}_{3.8}$ . The strength of our single crystals is higher than the strength of the polycrystals, what indicates that the defects and interfaces introduced by the fabrication procedure cause less detriment to the high temperature mechanical behavior than the grain boundaries in the polycrystalline material.

Creep tests were carried out in compression under constant load at temperatures of 1100 °C and 1300 °C, under nominal stresses ranging from 60 to 300 MPa (half of the strength was used in most of the creep experiments). The data recorded during creep were the instantaneous length versus time at constant load and temperature.

At 1100 °C and 1300 °C there is evidence of plastic behavior in the stress versus strain curves, with typically an acceleration of the creep rate before failure at 1100 °C. At 1300 °C, however, the creep rate reached a saturation in most cases and the strain versus time plot was rocky (Fig. 25). The creep behavior of the systems was very similar when a stress equal to half of the compressive strength was used (Fig. 25). This fact confirms the good mechanical behavior of  $\text{Sr}_3(\text{Ca}_{1.18}\text{Nb}_{1.82})\text{O}_{9.8}$  and  $\text{SrZr}_{0.9}\text{Y}_{0.1}\text{O}_{3.8}$  that, under a stress between two to three times higher than the other compounds, have the same creep behavior.  $\text{SrZr}_{0.9}\text{Y}_{0.1}\text{O}_{3.8}$  showed a remarkable long time to failure while all the other systems failed approximately at the same time. The strain to failure was approximately 3% in all the cases but for  $\text{SrCe}_{0.8}\text{Y}_{0.2}\text{O}_{3.8}$  the strain reached 8 %.

The creep resistant of our single crystals is also superior to the one from the polycrystalline materials. Fig. 26 shows a plot of the average strain rate versus stress for our systems together with data from Park et al. in polycrystalline  $\text{BaCe}_{1-x}\text{Y}_x\text{O}_{3.8}$ . The deformation mechanism in these polycrystals, grain boundary sliding, is not active in our systems. This fact explain the better creep behavior of directionally solidified materials. Other microscopic mechanisms, intrinsic to single crystals, dislocation or diffusion controlled, must be active in the materials studied in this work.



### **Microstructure after the mechanical tests**

After the mechanical tests, the samples were studied by SEM. Fig 27 shows micrographs of  $\text{SrCe}_{0.9}\text{Y}_{0.1}\text{O}_{3-\delta}$  deformed at 1300 °C. Fracture seems to propagate in its initial stages following the intergranular phase (Fig. 27 A), and, after a critical dimension was reach (Fig. 27 B), it can cut trough the grains. The amorphous intergranular phase is the weakest region and may control strength and creep resistance. Figure 21 C shows a top view of a crack where the typical features are also evident.

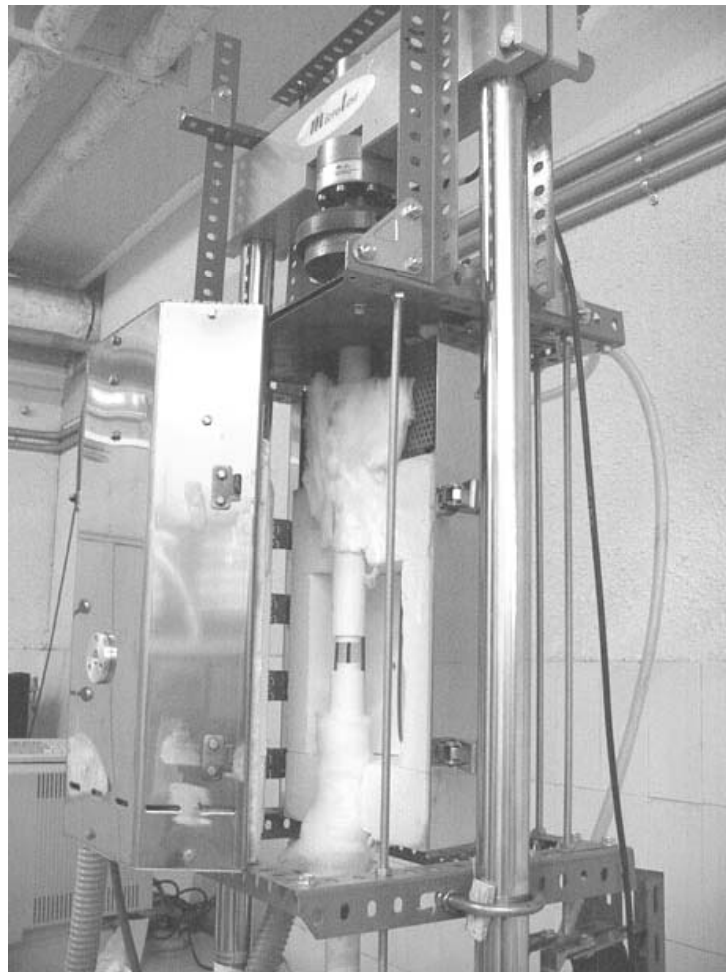


Fig. 21 –Equipment used to run the high temperature compression tests

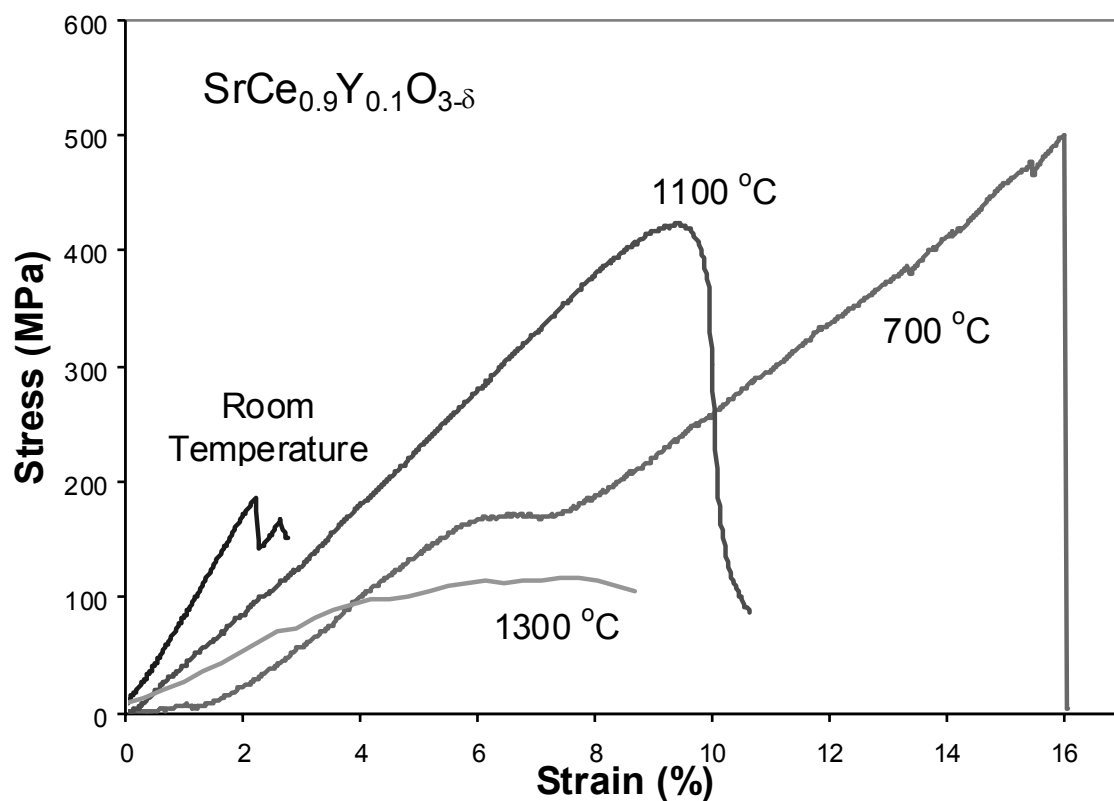


Fig. 22 – Stress versus strain curves of  $\text{SrCe}_{0.9}\text{Y}_{0.1}\text{O}_{3-\delta}$  deformed in compression at constant strain rate for a range of temperatures in air.

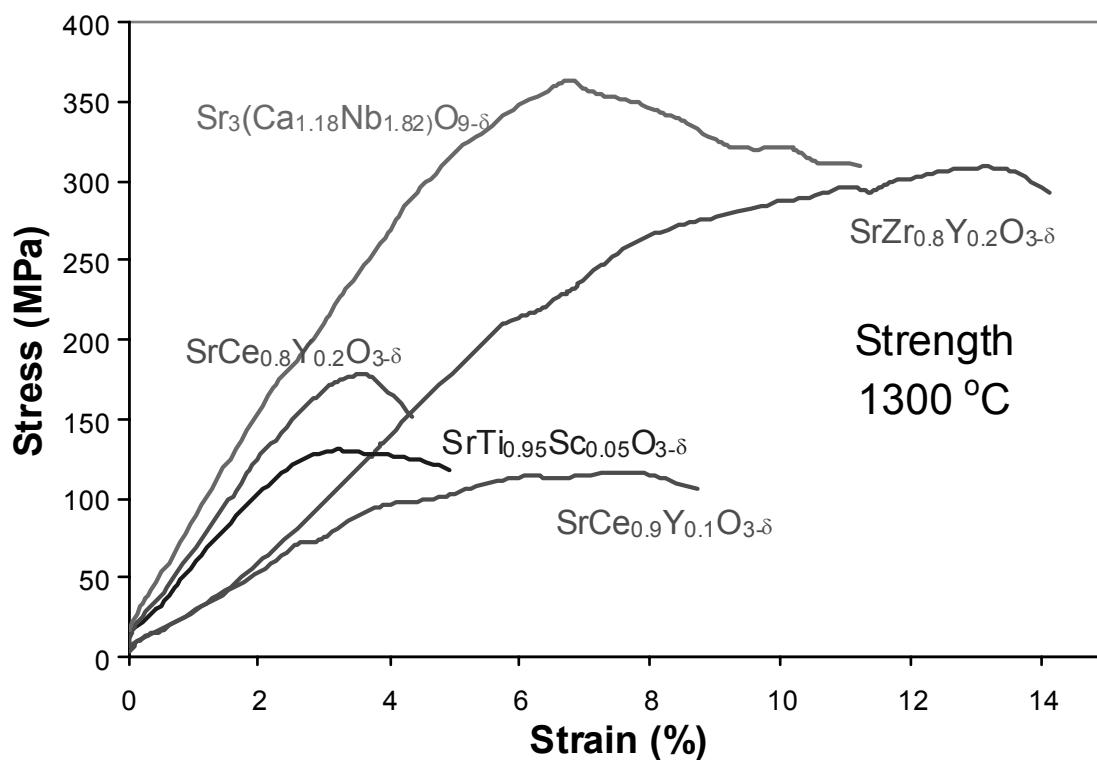


Fig. 23 – Stress versus strain curves of constant strain rate compression tests run at 1300 °C for all the materials studied in this work

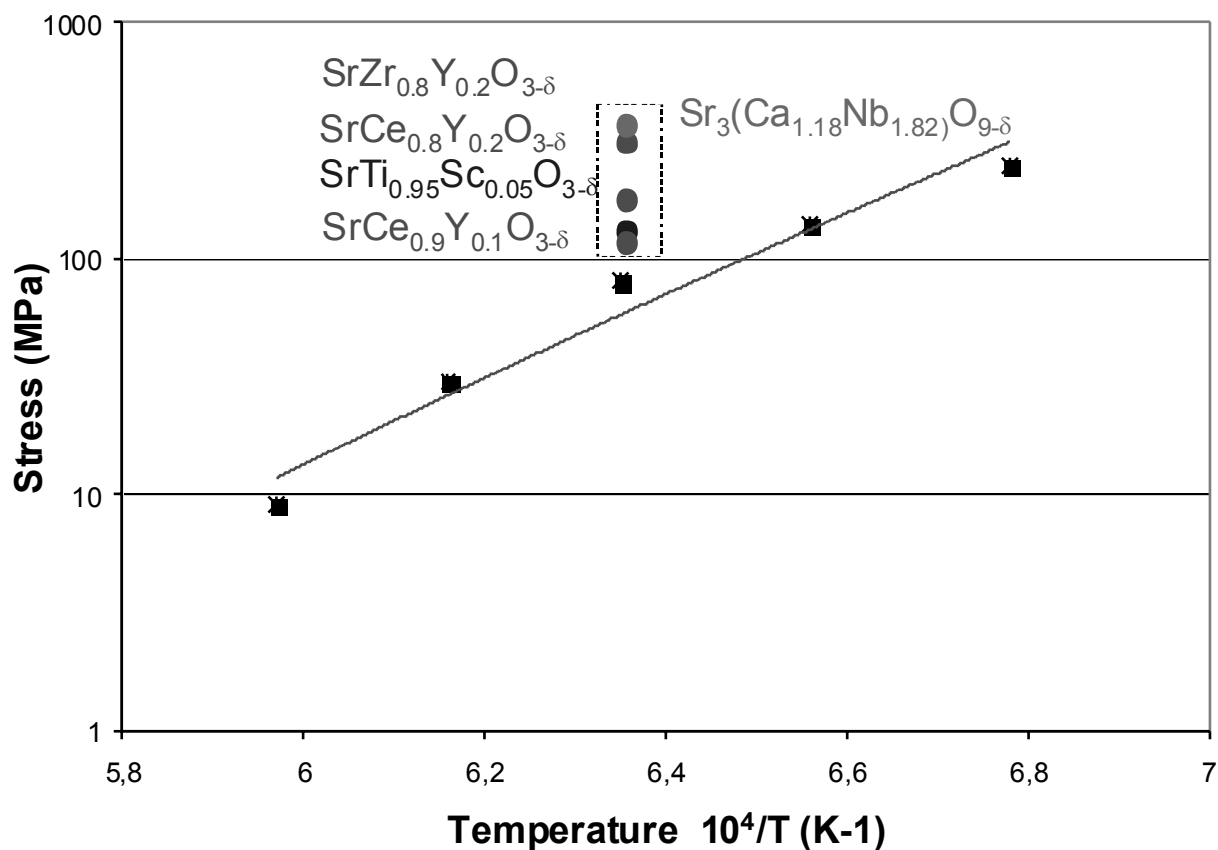


Fig. 24 – Strength versus temperature of the directionally solidified (studied in this work, indicated with a dashed line) and polycrystalline protonic conductors (Park et al.).

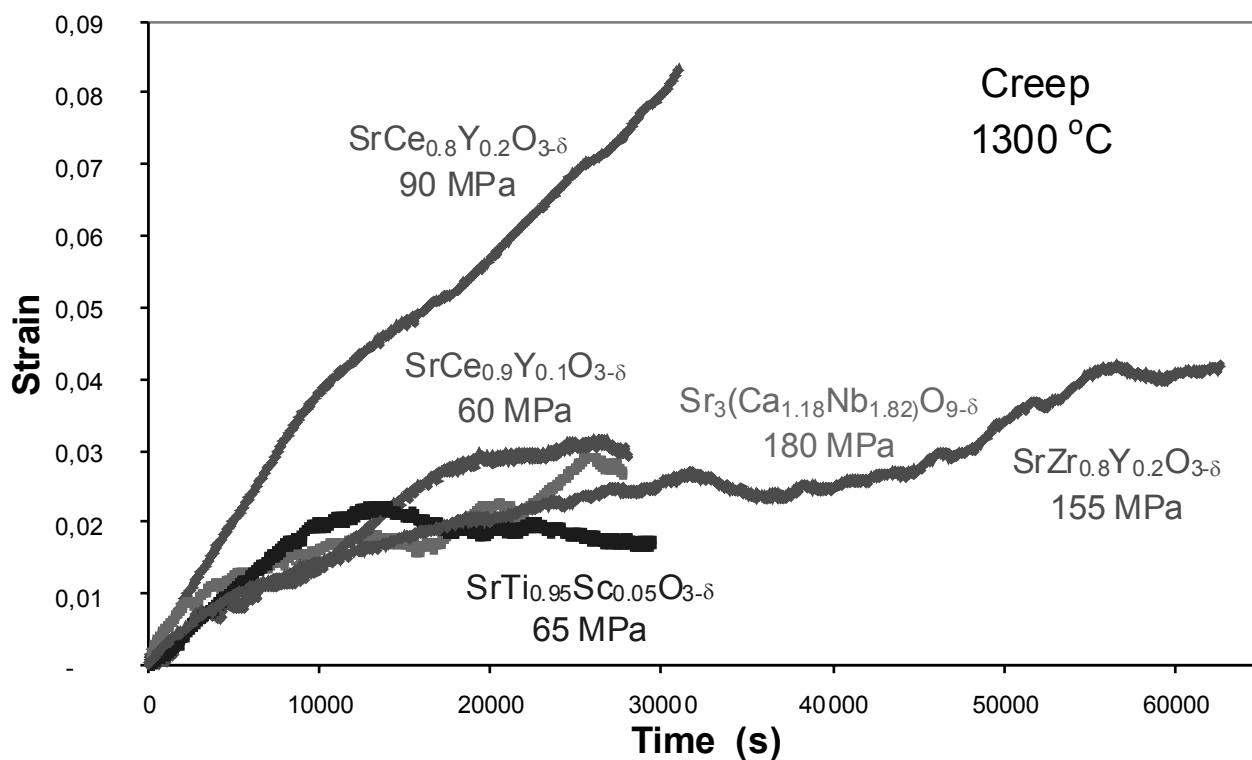


Fig. 25 – Strain versus time plots of the high temperature creep tests.

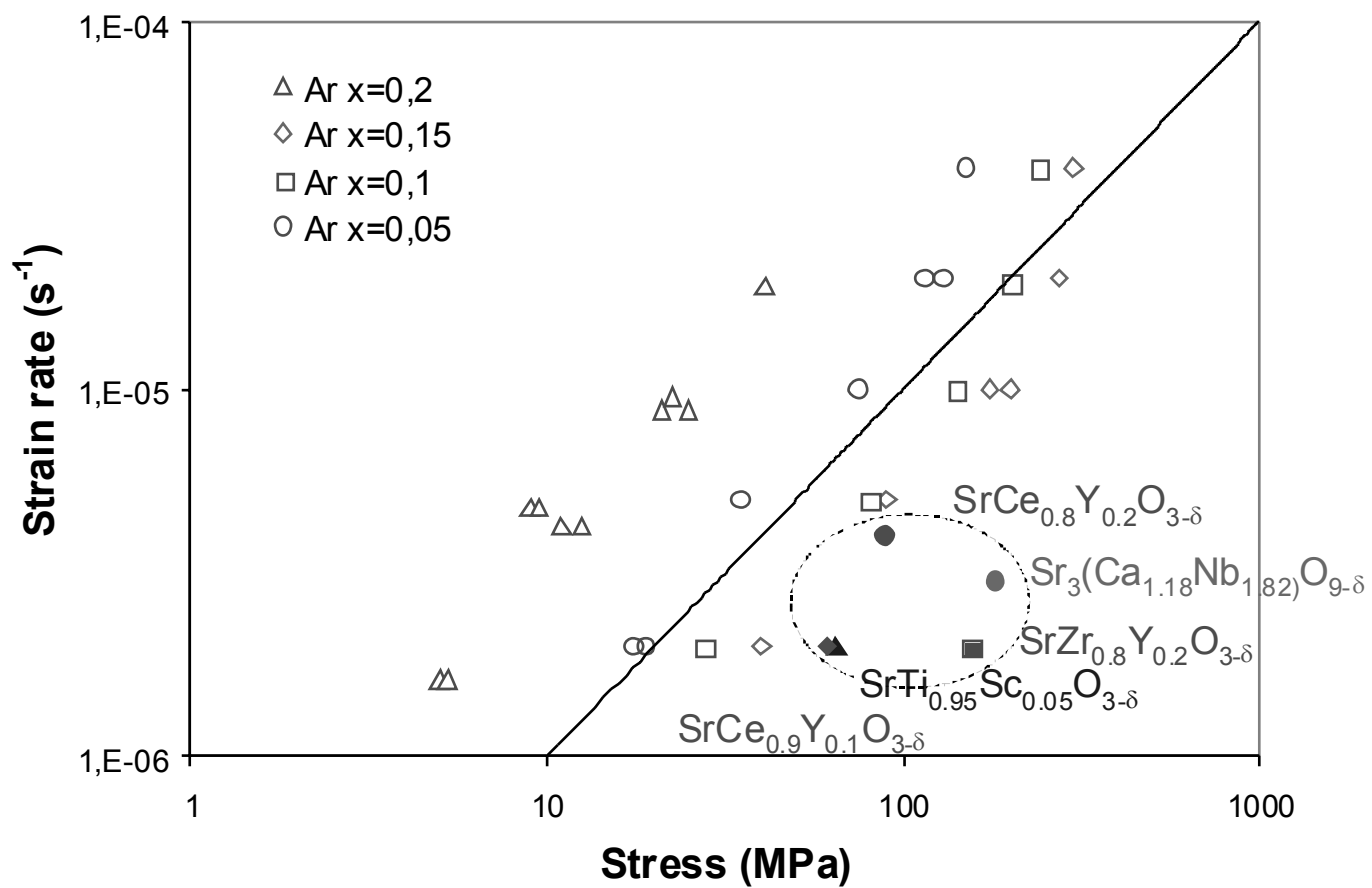
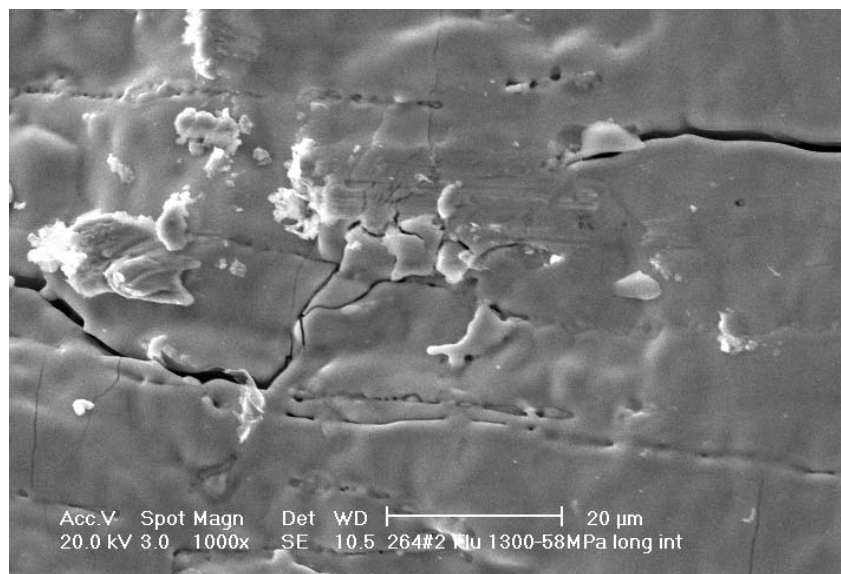
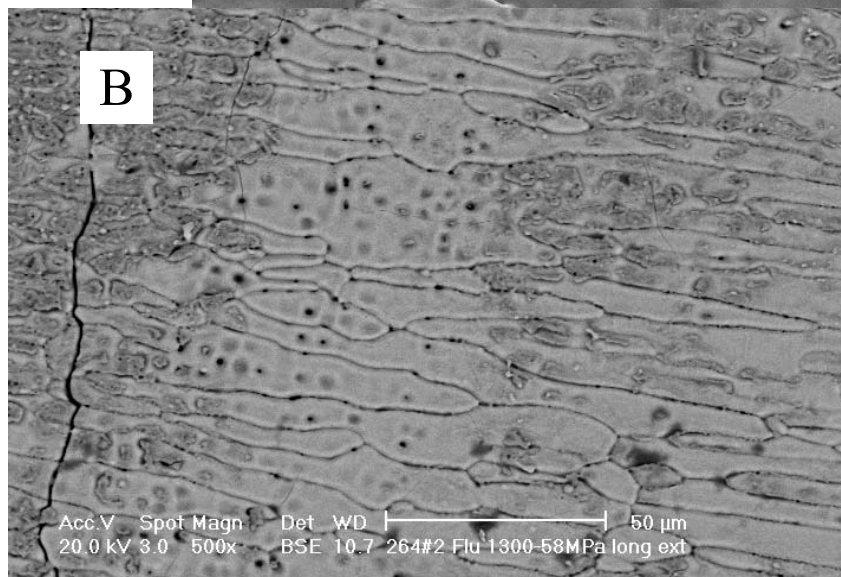


Fig. 26 – Strain rate versus stress of the directionally solidified (studied in this work, indicated with a dashed line) and polycrystalline protonic conductors (Park et al.).

A



B



C

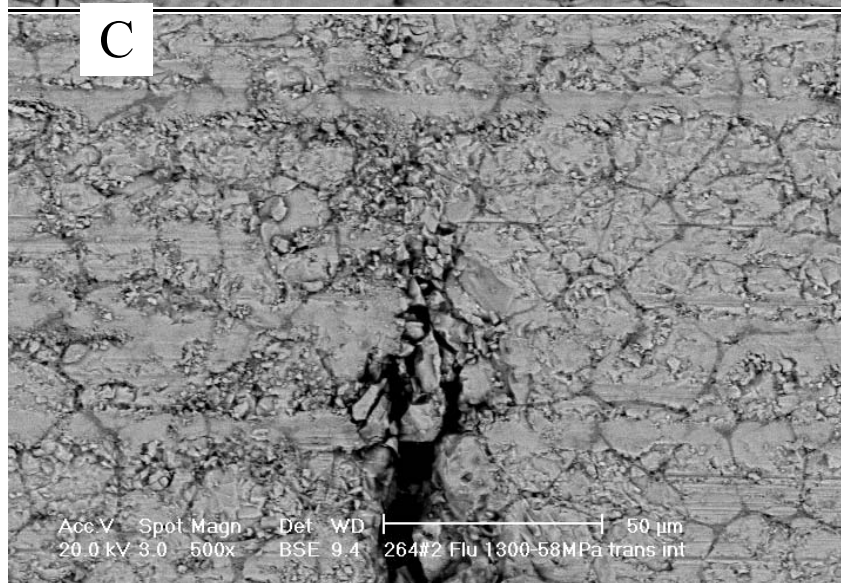


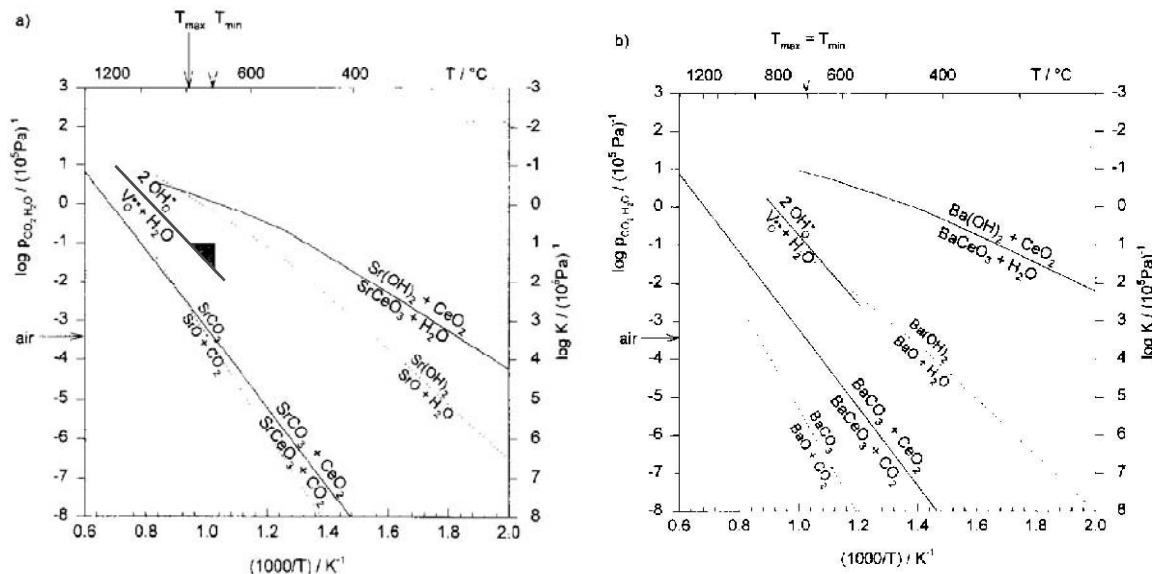
Fig 27 – SEM micrographs of  $\text{SrCe}_{0.9}\text{Y}_{0.1}\text{O}_{3-\delta}$  deformed at 1300 °C.

## Proton incorporation in HTPC

To study the incorporation of proton into the HTPC by nuclear microprobe analysis, vapour water heat treatment was achieved.

The sample chosen was a polished section of sample #264 ( $\text{SrCe}_{0.9}\text{Y}_{0.1}\text{O}_{3-\delta}$ ).

The temperature of the first heat treatment,  $700^\circ\text{C}$ , was chosen after a bibliographic study:  $600^\circ\text{C}$  is the temperature mainly used for  $\text{BaCeO}_3$ . The hydration of  $\text{SrCeO}_3$  is mainly done at  $800^\circ\text{C}$ .



Phase equilibria and defect equilibrium for hydration reaction for  $\text{SrCeO}_3$  and  $\text{BaCeO}_3$   
 Kreuer Solid state ionics 1997 **97** pp 1-45.

Iwahara et al. Solid state Ionics 79 (1995) 178 : preparation of Ca-doped  $\text{BaCeO}_3$  before electrical property measurements:

In this experiment, a column (diameter: 6 mm, thickness: 1 mm) of the specimen ceramic was used which was previously equilibrated with the atmosphere of wet argon gas at  $600^\circ\text{C}$

Kreuer et al. Solid state Ionics 86-88 (1996) 620 : preparation of Y-doped  $\text{BaCeO}_3$  before electrical property measurements:

Fixed water contents were adjusted by equilibrating the samples with the appropriate water partial pressure at  $600^\circ\text{C}$  before quenching in situ and measuring the a.c.-impedance in pure nitrogen ( $5\text{N}$ ) in the temperature range  $50\text{--}350^\circ\text{C}$ .

Phillips et al. Solid State Ionics 125 (1999) 393  $\text{SrCe}(\text{Y})\text{O}_3$  :

electrical conductivity, determined as a function of  $P_{O_2}$ , at  $T = 800^\circ\text{C}$  and  $P_{H_2O} = 0.007 \text{ atm}$

Reichel et al. Solid State Ionics 86-88 (1996) 640  $\text{SrCe(Y)O}_3$

the *protonic* conductivity observed for  $\text{SrCe}_{0.95}\text{Y}_{0.05}\text{O}_3$  at  $1073 \text{ K}$  and  $p_{H_2O} = 2 \cdot 10^3 \text{ Pa}$

Flowing wet air was not used because of water condensation on the cold parts of the heating elements of the furnace.

The sample was placed inside a stainless tube (dimension:  $H=2\text{cm}$ ,  $R_{\text{ext}}=10\text{cm}$ ,  $e=2\text{mm}$ ), and fixed with a nickel grid as seen in Fig 28 and 29. A volume  $v=0.1 \text{ cm}^3$  of water was poured inside the tube, which was then sealed.

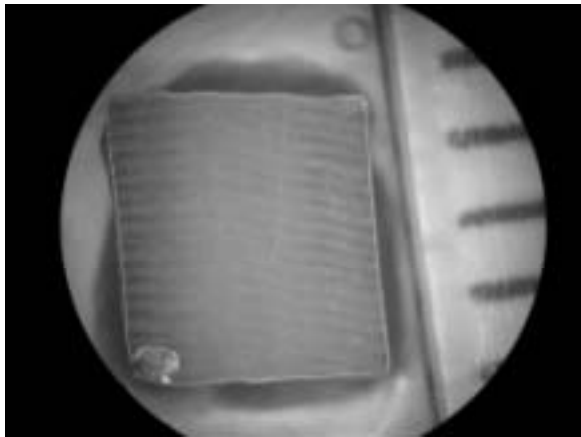


Fig 28 : polished section of sample 264  
scale bar: 1mm

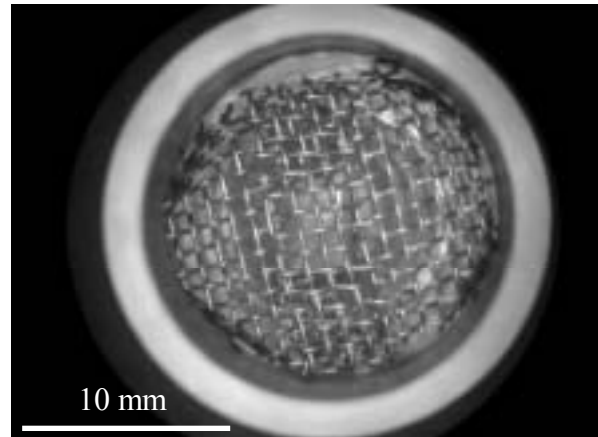


Fig 29 the sample is placed in a stainless tube  
fixed in a nickel grid.

The internal pressure built at  $700^\circ\text{C}$ ,  $P_{\text{tot}}(700^\circ\text{C})$ , was calculated using the following equations:

$$P_{\text{tot}}(700^\circ\text{C}) = p_{\text{air}}(700^\circ\text{C}) + p_{H_2O}(700^\circ\text{C})$$

$$p_{H_2O} = \frac{nRT}{V} = 11.2 \text{ MPa} = 112 \text{ bars where}$$

-V is the internal volume of the tube  $= 4 \cdot 10^{-6} \text{ m}^3$

-n number of moles is given by the volume of water  $v$  in  $\text{cm}^3$ ,  $n = v/18 = 0.0055$

- $R = 8.31 \text{ m}^3 \cdot \text{Pa} / \text{mol} \cdot \text{K}$

$$p_{\text{air}}(700^\circ\text{C}) = 10^5 \cdot \frac{273+700}{273+25} \text{ Pa} = 0.33 \text{ MPa} = 3.3 \text{ bars} (<< p_{H_2O})$$

$$P_{\text{tot}} = 11.5 \text{ MPa} (115 \text{ bars})$$

It was checked that the pressure developed on the tube,  $P = P_{\text{tot}} \cdot \frac{R_{\text{ext}}}{e} = 57 \text{ MPa}$ , is lower than the limit of elasticity of stainless steel ( $\approx 200 \text{ MPa}$ )

Fig 30 presents the  $\text{SrCe}_{0.9}\text{Y}_{0.1}\text{O}_{3-\delta}$  sample after the water heat treatment with the above-mentioned conditions, for one hour. Fig 31 shows that the decomposition persisted in ambient air at room temperature. The sample was dissociated presumably into  $\text{Sr}(\text{OH})_2$  and  $\text{CeO}_2$  due to a too high vapour pressure in the tube.

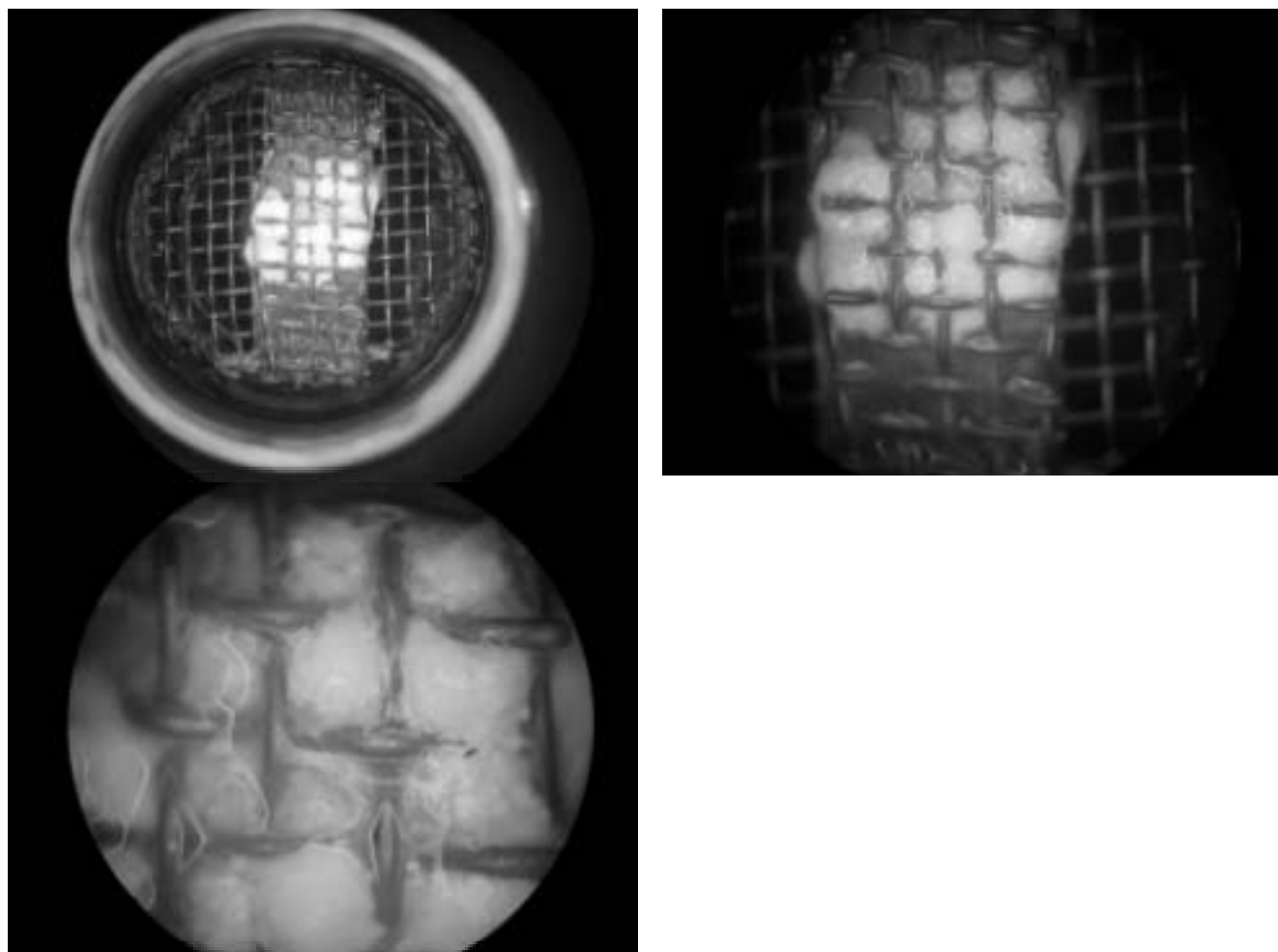


Fig 30 aspect of the sample immediately after the test

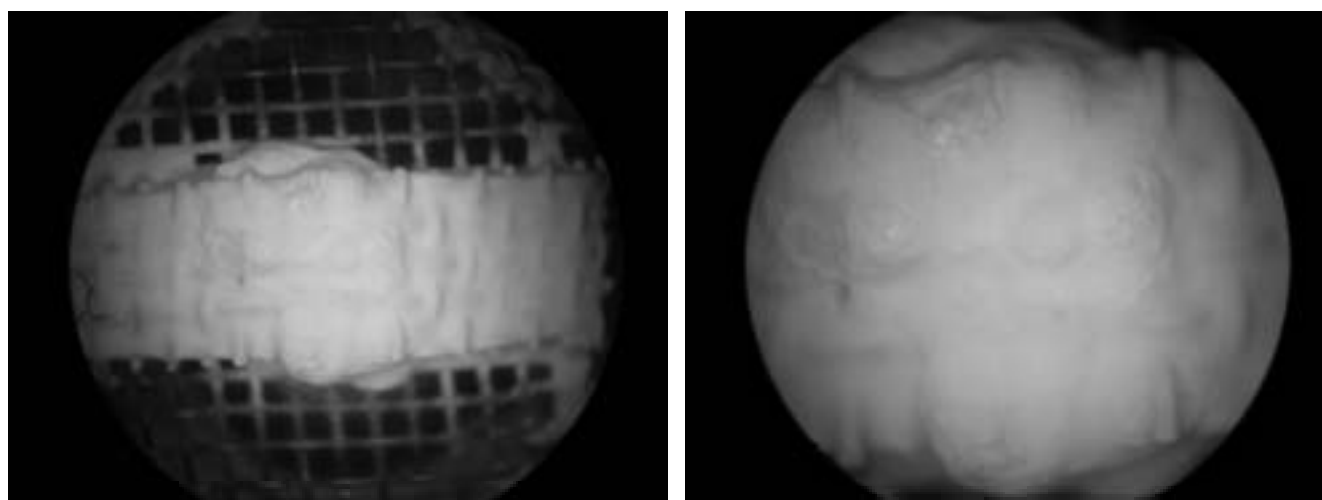


Fig 31: Aspect after 5 days in air at 25°C



The next vapour treatments had to be conducted under lower vapour pressure.

The amount of water absorbed on the inner wall of the cylinder has been evaluated knowing that around  $10^{17}$  water molecules per  $\text{cm}^2$  are adsorbed on a metallic surface.

The internal surface of the closed tube is  $S = H \cdot 2\pi R_{\text{int}} + 2 \cdot \pi R_{\text{int}}^2 \approx 14 \text{ cm}^2$   
( $H=2\text{cm}$ ,  $R_{\text{int}}=0.8\text{cm}$ )

The number of moles  $n$  is then  $n = (14 \cdot 10^{17}) / (6.023 \cdot 10^{23}) \approx 2.3 \cdot 10^{-6}$ .

The pressure in the tube at  $700^\circ\text{C}$  is  $P \approx nRT/V \approx 4.4 \cdot 10^4 \text{ Pa}$ .

The water adsorbed in the inner wall of the cylinder build is sufficient to place the sample in the pressure domain in which proton can be introduced and at the boundary limit for decomposition into  $\text{Sr}(\text{OH})_2 + \text{CeO}_2$ .

The samples #264 ( $\text{SrCe}_{0.9}\text{Y}_{0.1}\text{O}_{3-\delta}$ ) and #271 ( $\text{Sr}_3(\text{Ca}_{1.18}\text{Nb}_{1.82})\text{O}_{9-\delta}$ ) have been heat treated at  $700^\circ\text{C}$  in a closed tube ( $H=2\text{cm}$ ,  $R_{\text{int}}=0.8\text{cm}$ ). After the treatment, the internal wall had bluish reflection and the sample 264 was darker. No macroscopic decomposition of the samples was noticed.

Figure 32 and 33 presents optical micrographs of the sample #271 ( $\text{Sr}_3(\text{Ca}_{1.18}\text{Nb}_{1.82})\text{O}_{9-\delta}$ ) after heat treatment. This sample will be used for nuclear microprobe analysis. A core/surface texture is noticeable.

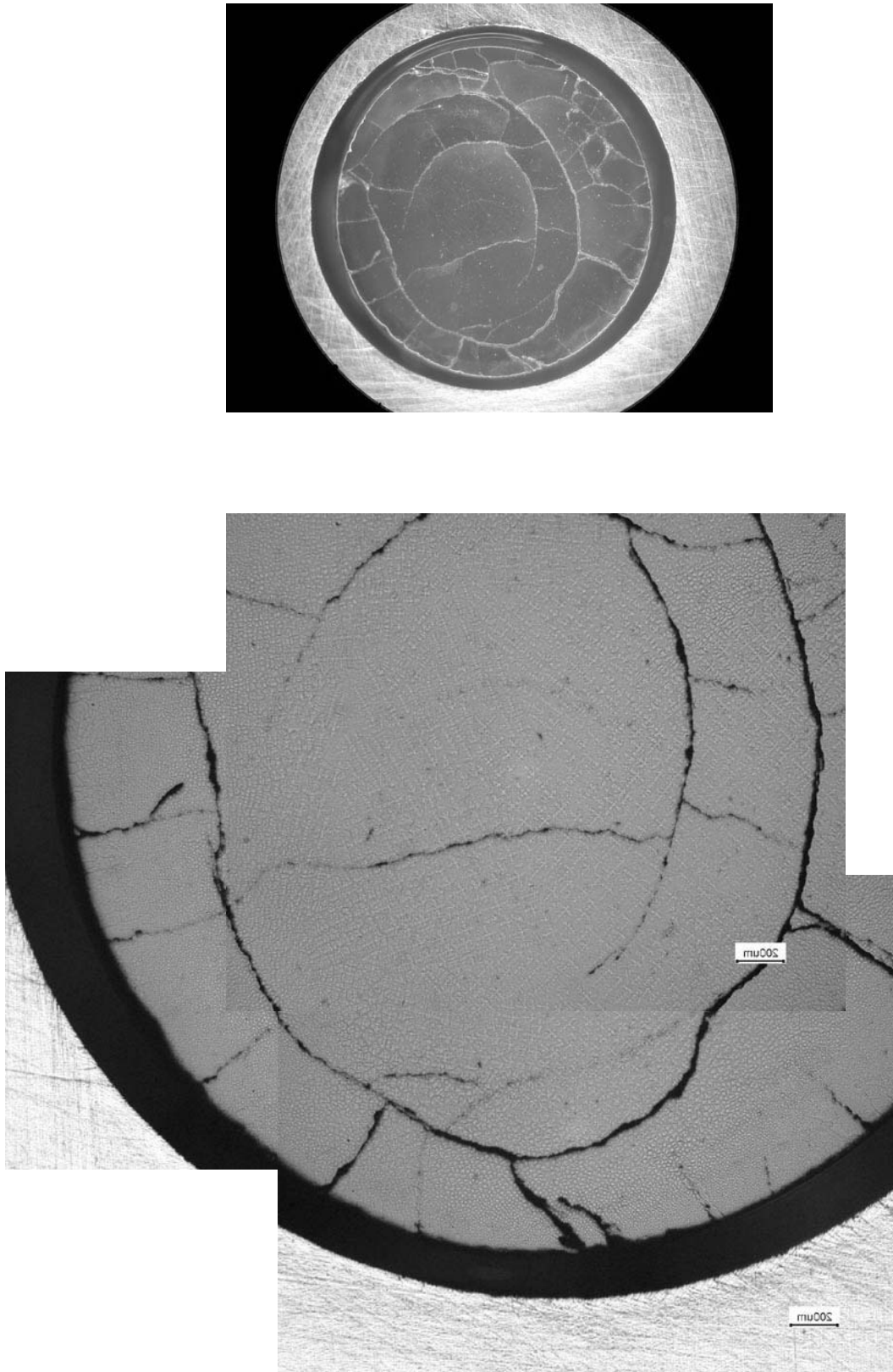


Fig 32: Sample 271 ( $\text{Sr}_3(\text{Ca}_{1.18}\text{Nb}_{1.82})\text{O}_{9.8}$ ) after heat treatment.

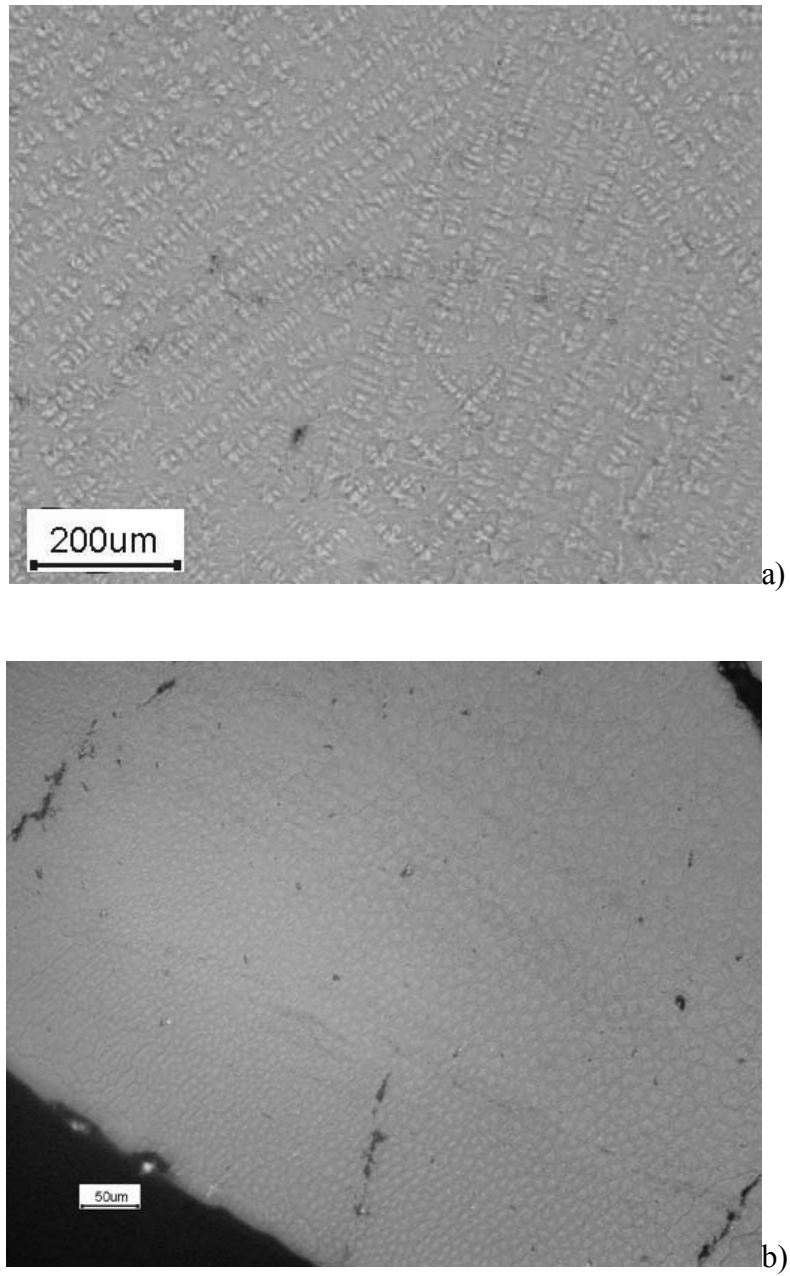


Fig 33: Sample 271 ( $\text{Sr}_3(\text{Ca}_{1.18}\text{Nb}_{1.82})\text{O}_{9.6}$ ) after heat treatment. a) core, b) outer part

## **Impedance spectroscopy**

The electrical characterization of the protonic conductors developed in this project is achieved through impedance measurements at high temperature and modified environment.

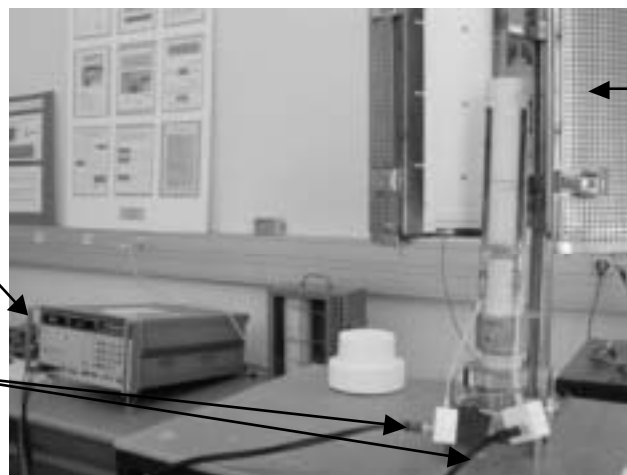
During this year, a dedicated furnace has been developed including gas inlet and electrical connections. Connections have to withstand high temperature and to be correctly screened to permit high frequency measurements and provide low contact resistance.

A general view of the equipment is shown in Fig 34. The furnace (AET Technologies) is composed of a FeCr AlCo winding (Kanthal APM) embedded in an alumina cement. Its maximum temperature is 800°C. A hollowed alumina tube is positioned at the center of the furnace. On the top of this tube is screwed an alumina chamber receiving the sample to analyze, as shown in Fig 35. Platinum ink is deposited on the two sides of the sample to fix two platinum connectors. Each connector is then wound around two platinum wires, one for the imposed voltage, one for the current measurement. These wires are inserted into alumina tubes (those used for thermo-couples), which are in turn inserted into copper tubes for electrical screening (Fig 35 and 36). The final connections to the spectrometer are achieved through coax cables. The specimen chamber can be subjected to gas flow. Gas is inserted from the bottom of the alumina tube, Fig 37, up to the hollowed specimen chamber. For the highest temperatures of tests, the metallic/alumina connections used for the gas inlet require water-cooling to avoid thermal stress and failure of the alumina tube.

Fig 38 shows an example of spectrum at 400°C in ambient air on  $\text{Sr}_3(\text{Ca}_{1.18}\text{Nb}_{1.82})\text{O}_{9.8}$ . The sample is a disk of 4 mm in diameter and 1.5 mm in thickness. The right part of the curve corresponds to the contribution of the electrodes, at the lowest frequency. From last part of the curve, the impedance of the boundary+grain system can be deduced. This curve is comparable to that published by Haile et al., Fig 39. The separation of the contribution of the grains from that of the grain boundary will be possible at lower temperature. Our first attempts to produce results at lower temperature were not successful presumably because of insufficient quality of electrical contacts. During the next months, we will improve the contact resistances and conduct tests under wet air.

Impedance  
spectrometer  
HP 4192  
5 Hz to 13 MHz

Connections to the  
spectrometer



Furnace

Fig 34: general view of the device for impedance measurement at high temperature.

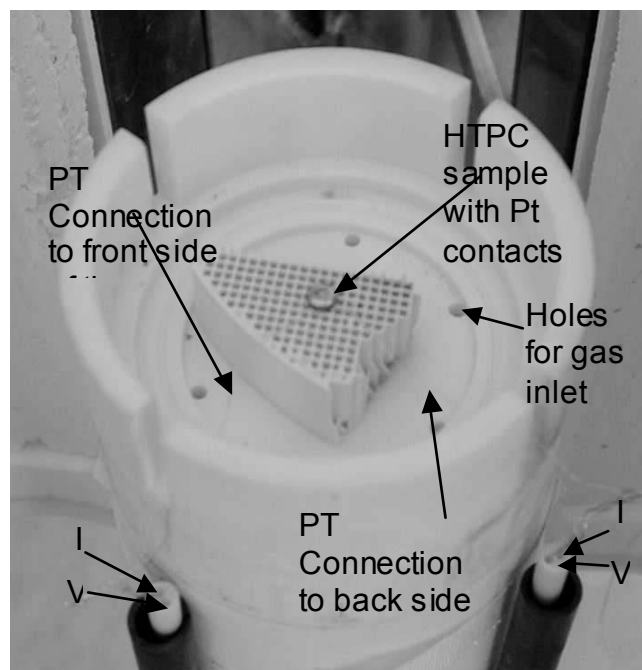


Fig 35: specimen chamber (opened).

Electrical connections :  
Pt wire  
placed inside  
an alumina  
tube with 2  
holes,  
surrounded by  
a copper tube

Imposed  $V \sim$

Measured  $I \sim$

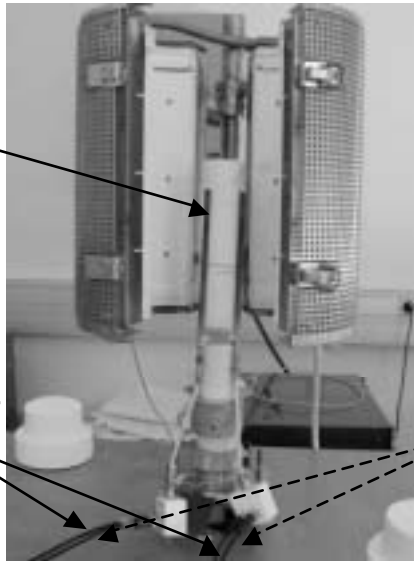


Fig 36: Electrical connections

Furnace

Water  
cooling  
system

Gaz inlet  
(ex : wet air)

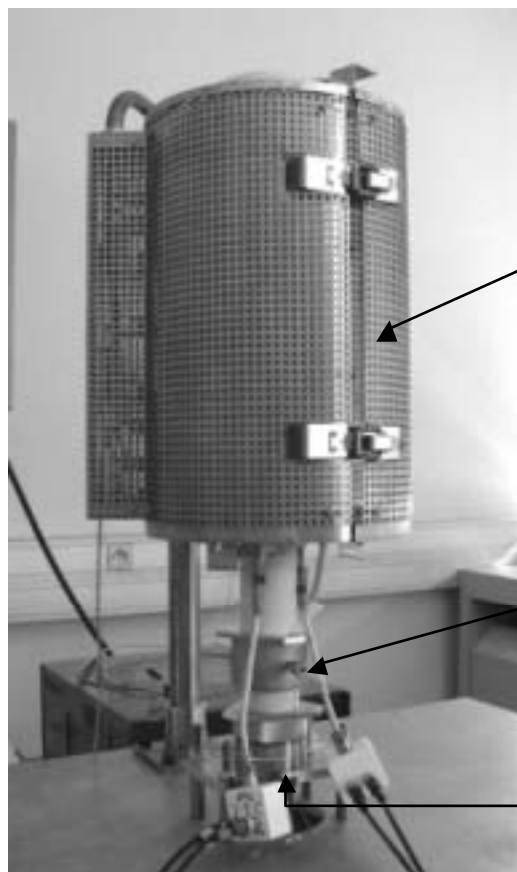


Fig 37- Furnace in the operating closed position.

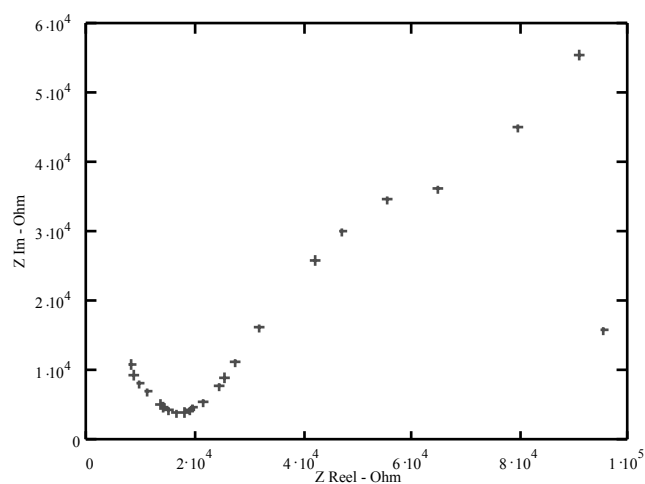


Fig 38 : Impedance spectrum of  $\text{Sr}_3(\text{Ca}_{1.18}\text{Nb}_{1.82})\text{O}_{9-\delta}$  at  $400^\circ\text{C}$  in ambient air

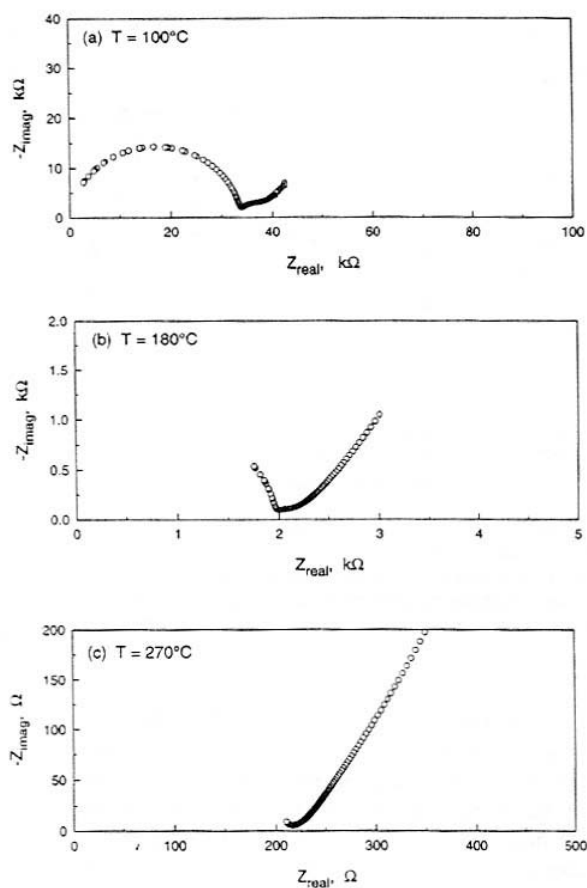


FIG. 13. (a–c) Nyquist impedance plots obtained for batch-2 samples of  $\text{BaCe}_{0.85}\text{Gd}_{0.15}\text{O}_{3-\delta}$  sintered at  $1700^\circ\text{C}$ . Temperature of the measurement as indicated. Atmosphere is  $\text{H}_2\text{O}$ -saturated argon. Unlike the situation reflected in Fig. 12,  $R_2$  becomes negligible in (c) such that the total resistance is approximately  $R_1$ .

Fig 39 : Haile SM , West D.L/, Campbell J. J. Mater Res **13** [6] 1998.  
 $\text{BaCe}_{0.85}\text{Gd}_{0.15}\text{O}_{3-\delta}$  - measurement in  $\text{H}_2\text{O}$  saturated argon.

## Nuclear Microprobe measurements

Nuclear microprobe was applied to investigate two samples of each family,  $\text{SrCe}_{0.9}\text{Y}_{0.1}\text{O}_{3-\delta}$  (simple perovskite, n° 264 ) and  $\text{Sr}_3(\text{Ca}_{1.18}\text{Nb}_{1.82})\text{O}_{9-\delta}$  (mixed perovskite, n° 271). The experimental conditions (particle type:  $^4\text{He}^+$ , energy: 3.06 MeV, surface barrier particle detectors: standard at  $30^\circ$  and annular at  $170^\circ$ ) were chosen to fit to ERDA requirements (Elastic Recoil Detection Analysis) for hydrogen detection. When possible, RBS (Rutherford BackScattering) and PIXE (Particle Induced X-ray Emission) (Ge(hp) EDS detector) were also performed.

Each map has been recorded in a two step process: 1°) sample perpendicular to the ion beam to investigate the composition by RBS and PIXE. 2°) sample tilted at  $75^\circ$  for hydrogen determination by ERDA. In the latter case, RBS is still performed to monitor the beam dose but not for analytical use.

### Sample #264

Investigations are related to zone 3, corresponding to the core of the rod (cf. microstructure section) after the water heat treatment. In a standard RBS spectrum, the height of a step and its intensity variation with the energy give information on the surface concentration and in-depth profile, respectively. The height of the step is proportional to the concentration of the element and to the square of its atomic number. As the energy shift from the right side of the step corresponds to a depth scale from the surface, in-depth modifications of the concentrations may be evidenced. A homogeneous  $\text{SrCe}_{0.9}\text{Y}_{0.1}\text{O}_{3-\delta}$  sample would give rise to the simulated spectrum shown in bold in fig.40, which shows the foreseen relative heights of the Ce and Sr+Y steps (Sr and Y are not mass separated). In addition, a homogeneous concentration must lead to nearly flat steps.



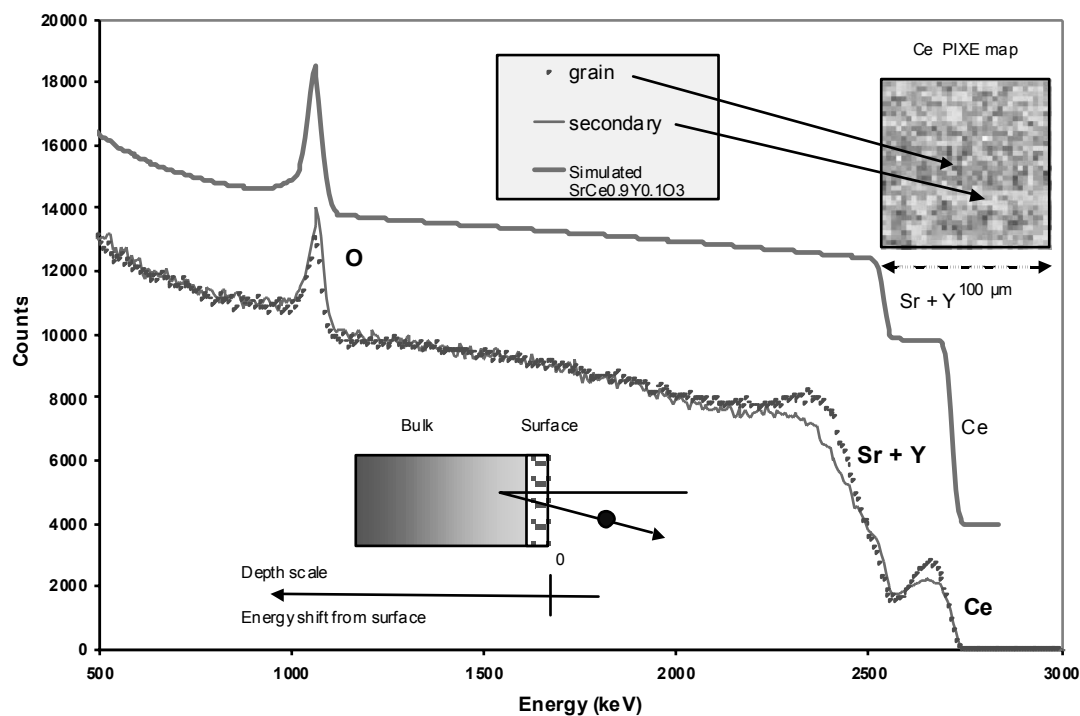


Figure 40 : RBS spectra of grains and intergranular secondary phase in sample #264 after water heat treatment (+ PIXE map of Ce).

The experimental RBS spectra obtained on #264 evidence a strong alteration of the surface. The surface Ce/(Sr+Y) ratio is close to 0.2 and the Ce concentration decreases from the surface towards the bulk of the sample. This may be interpreted as a selective leaching of Ce accompanied by a re-precipitation, since both a Ce depletion from the bulk composition and a surface enrichment are observed. The whole thickness of the altered layer may be estimated from the spectrum between 300 and 500 nm. At higher depth, the composition remains unchanged as demonstrated by electron microprobe measurements.

PIXE maps confirm Ce depleted composition of the intergranular secondary phase and the corresponding RBS spectra show a differentiated alteration of the grains and of the boundaries (cf. fig. a).

An ERDA spectrum has to be read like a RBS spectrum. Indeed, the spectrum of sample with an homogeneous hydrogen distribution appears as a step with a more or less steeply slope (cf. spectrum on fig 41 of a kapton® polymer foil used as a qualitative standard). Evolutions of the intensity with the energy shift from the surface reflect the hydrogen depth profile.

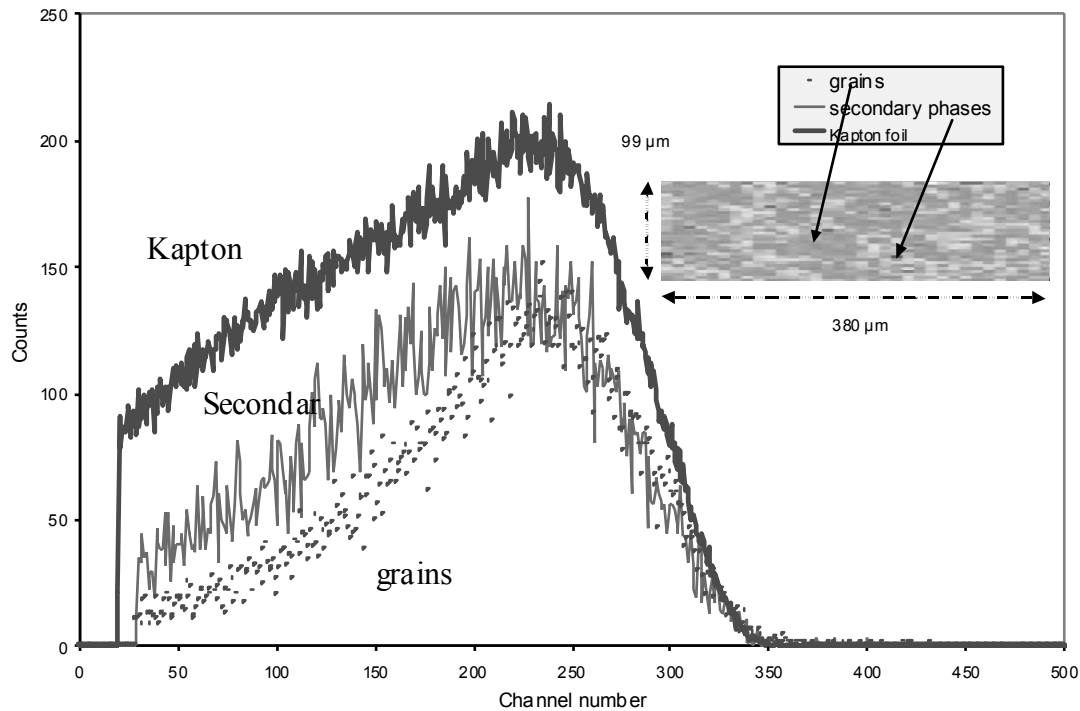


Figure 41: ERDA spectra of a kapton® foil, grains and secondary intergranular phase in #264 sample.

The ERDA spectra obtained from both grains and secondary intergranular phase show a high hydrogen content, especially for the secondary phase. However, the probe depth is limited to first 100 nm and reflects only the hydrogenation of the altered layer. A transverse cut after water heat treatment would be necessary to probe bulk hydrogen transport properties.

#### Sample #271

Two samples have been investigated: raw and water heat treated. Compared to #264, the chemical stability of #271 is much better. On the treated sample, only a slight sign of surface alteration may be seen on RBS spectra (top of Sr+Nb step, cf fig.42), in the order of a few 10 nm. The simulation based on its nominal composition fits very well.

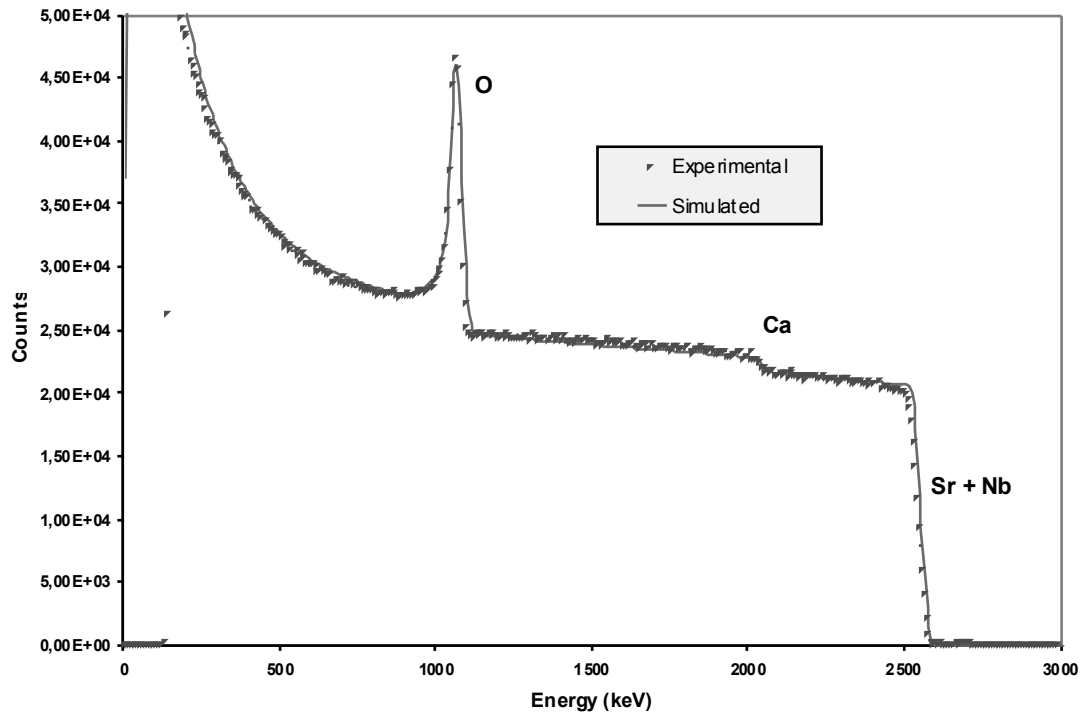


Figure 42: RBS spectrum of treated #271. Simulation for the nominal composition

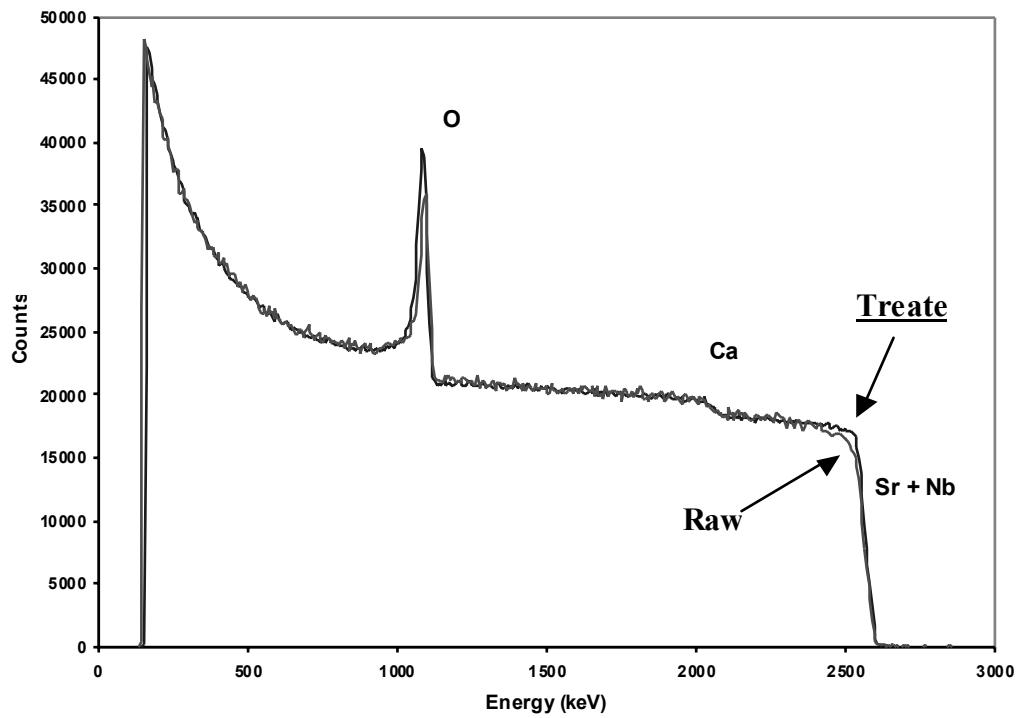


Figure 43: Experimental RBS spectra of raw and treated #271 samples

The comparison of the RBS spectra of raw (polished 3 weeks before) and treated (freshly polished before treatment) samples shows a more important surface alteration for a storage at room temperature than for a short water heat treatment (cf. fig 43). This tends to prove that the long term stability of this phase has to be evaluated and the mechanism of alteration to be investigated.

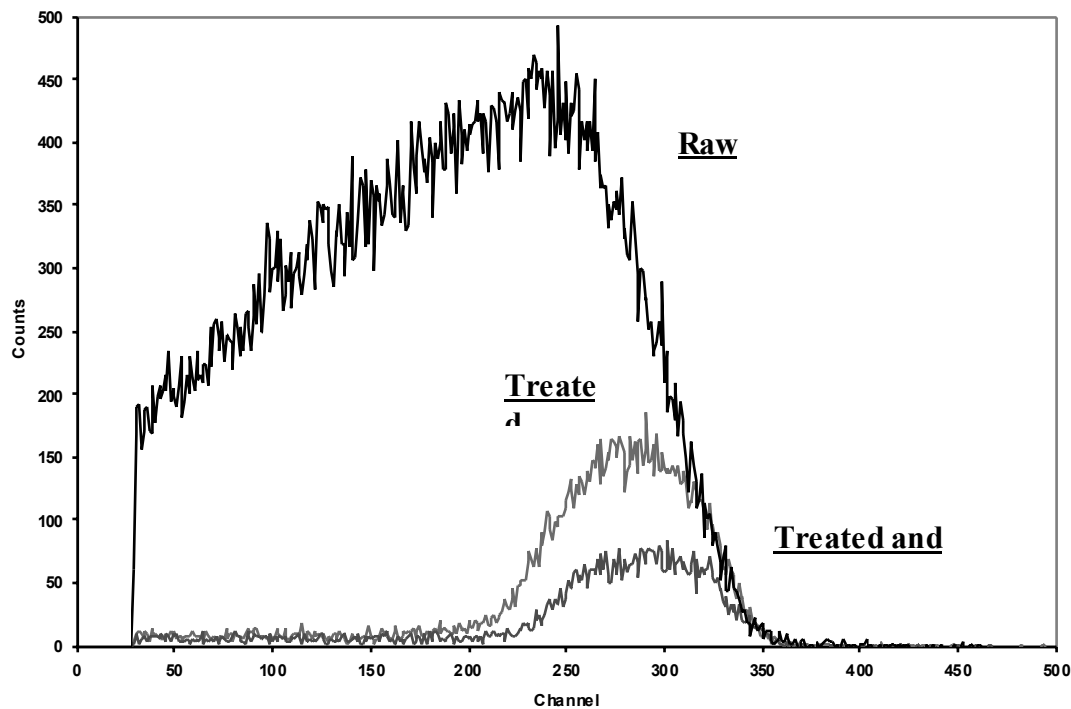


Figure 44 : ERDA spectra of #271 sample : raw, treated, treated and polished

The ERDA spectra confirm on one hand the strong surface hydrolysis of raw samples but on the other hand the limited alteration of freshly treated ones (cf. fig 44). In addition, a further mechanical polishing after the water heat treatment to remove the altered surface layer do not introduce a new thick hydrated layer which may interfere in the low energy part of the spectrum, preventing from hydrogen quantitative analysis. Further quantitative mapping of bulk hydrogen will be then possible from cross sections elaborated after the water treatment.

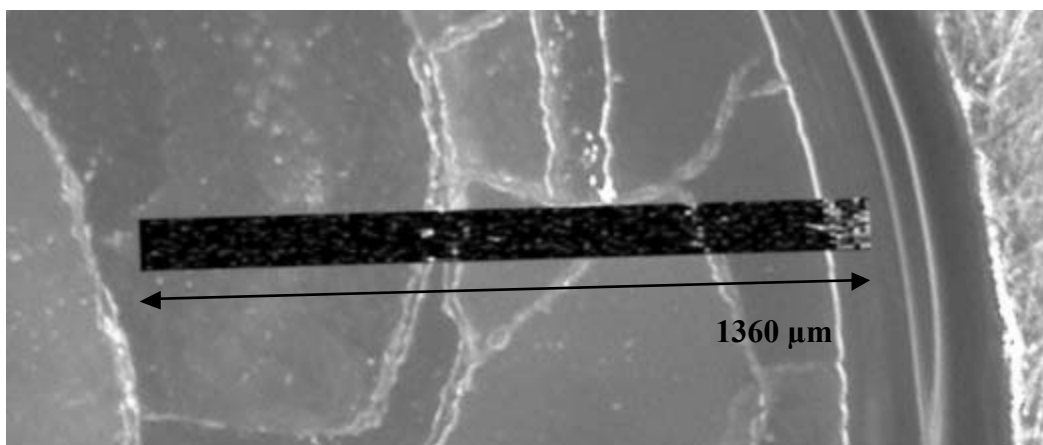


Figure 45 : ERDA map of treated #271 sample

ERDA mapping of the treated surface (Fig. 45, transverse cross section) do not evidence any difference of chemical reactivity from the core to the surface of the rod. The only contrast in hydrogen mapping comes from the cracks and may be due to a geometrical effect rather than a local hydrogen over-concentration.

#### Conclusions on nuclear microanalysis

##### - #264

The water heat treatment strongly alters the surface. From RBS measurements, both Ce depletion and surface re-deposition is evidenced. The thickness of the modified layer is between 300 and 500 nm. In spite of depth profiling capabilities, ERDA measurement directly from the treated surface may only probe the altered layer because of the probed depth limited to the first 100 nm.

##### - #271

RBS measurements show a good chemical stability under water heat treatment, but the long term stability remains questionable. First ERDA investigations on a treated cross section of a rod do not evidence difference in the hydrogen incorporation capabilities from the core to the surface of the rod.

##### - General

These preliminary tests have shown that both RBS and ERDA techniques may be successfully applied. However, to investigate bulk hydrogen transport properties, further measurements on cross sections, prepared after the water treatment, will be essential.

## **Conclusions**

- High temperature protonic conductors can be fabricated by directional solidification.
- These materials present a cellular structure with crystalline cells and an amorphous intergranular phase. The cell width ranges between 10-50  $\mu\text{m}$  and the aspect ratios are roughly up to 10. TEM and HRTEM confirmed the perovskite structure.
- The protonic conductors fabricated by these techniques have better strength and creep resistance than the sintered polycrystals. The best properties were achieved by the mixed perovskites with a strength of 370 MPa at 1300  $^{\circ}\text{C}$ .
- The mechanical properties study indicates that the high temperature protonic conductors fabricated by directional solidification can be used for temperatures up to 1300  $^{\circ}\text{C}$ .
- A procedure for proton incorporation was successfully developed.
- Impedance spectra were obtained. The behaviour being comparable to sintered polycrystals.
- RBS and ERDA techniques were successfully applied. To investigate bulk hydrogen transport properties, further measurements on cross sections, prepared after the water treatment, will be essential.